

Study of $e^+e^- \rightarrow p\bar{p}$ via initial-state radiation at BABAR

J. P. Lees,¹ V. Poireau,¹ V. Tisserand,¹ E. Grauges,² A. Palano,^{3a,3b} G. Eigen,⁴ B. Stugu,⁴ D. N. Brown,⁵ L. T. Kerth,⁵ Yu. G. Kolomensky,⁵ G. Lynch,⁵ H. Koch,⁶ T. Schroeder,⁶ D. J. Asgeirsson,⁷ C. Hearty,⁷ T. S. Mattison,⁷ J. A. McKenna,⁷ R. Y. So,⁷ A. Khan,⁸ V. E. Blinov,⁹ A. R. Buzykaev,⁹ V. P. Druzhinin,⁹ V. B. Golubev,⁹ E. A. Kravchenko,⁹ A. P. Onuchin,⁹ S. I. Serednyakov,⁹ Yu. I. Skovpen,⁹ E. P. Solodov,⁹ K. Yu. Todyshev,⁹ A. N. Yushkov,⁹ D. Kirkby,¹⁰ A. J. Lankford,¹⁰ M. Mandelkern,¹⁰ B. Dey,¹¹ J. W. Gary,¹¹ O. Long,¹¹ G. M. Vitug,¹¹ C. Campagnari,¹² M. Franco Sevilla,¹² T. M. Hong,¹² D. Kovalskyi,¹² J. D. Richman,¹² C. A. West,¹² A. M. Eisner,¹³ W. S. Lockman,¹³ A. J. Martinez,¹³ B. A. Schumm,¹³ A. Seiden,¹³ D. S. Chao,¹⁴ C. H. Cheng,¹⁴ B. Echenard,¹⁴ K. T. Flood,¹⁴ D. G. Hitlin,¹⁴ P. Ongmongkolkul,¹⁴ F. C. Porter,¹⁴ A. Y. Rakitin,¹⁴ R. Andreassen,¹⁵ Z. Huard,¹⁵ B. T. Meadows,¹⁵ M. D. Sokoloff,¹⁵ L. Sun,¹⁵ P. C. Bloom,¹⁶ W. T. Ford,¹⁶ A. Gaz,¹⁶ U. Nauenberg,¹⁶ J. G. Smith,¹⁶ S. R. Wagner,¹⁶ R. Ayad,^{17,*} W. H. Toki,¹⁷ B. Spaan,¹⁸ K. R. Schubert,¹⁹ R. Schwierz,¹⁹ D. Bernard,²⁰ M. Verderi,²⁰ P. J. Clark,²¹ S. Playfer,²¹ D. Bettoni,^{22a} C. Bozzi,^{22a} R. Calabrese,^{22a,22b} G. Cibinetto,^{22a,22b} E. Fioravanti,^{22a,22b} I. Garzia,^{22a,22b} E. Luppi,^{22a,22b} L. Piemontese,^{22a} V. Santoro,^{22a} R. Baldini-Feroli,²³ A. Calcaterra,²³ R. de Sangro,²³ G. Finocchiaro,²³ P. Patteri,²³ I. M. Peruzzi,^{23,†} M. Piccolo,²³ M. Rama,²³ A. Zallo,²³ R. Contri,^{24a,24b} E. Guido,^{24a,24b} M. Lo Vetere,^{24a,24b} M. R. Monge,^{24a,24b} S. Passaggio,^{24a} C. Patrignani,^{24a,24b} E. Robutti,^{24a} B. Bhuyan,²⁵ V. Prasad,²⁵ M. Morii,²⁶ A. Adametz,²⁷ U. Uwer,²⁷ H. M. Lacker,²⁸ T. Lueck,²⁸ P. D. Dauncey,²⁹ U. Mallik,³⁰ C. Chen,³¹ J. Cochran,³¹ W. T. Meyer,³¹ S. Prell,³¹ A. E. Rubin,³¹ A. V. Gritsan,³² N. Arnaud,³³ M. Davier,³³ D. Derkach,³³ G. Grosdidier,³³ F. Le Diberder,³³ A. M. Lutz,³³ B. Malaescu,³³ P. Roudeau,³³ M. H. Schune,³³ A. Stocchi,³³ G. Wormser,³³ D. J. Lange,³⁴ D. M. Wright,³⁴ J. P. Coleman,³⁵ J. R. Fry,³⁵ E. Gabathuler,³⁵ D. E. Hutchcroft,³⁵ D. J. Payne,³⁵ C. Touramanis,³⁵ A. J. Bevan,³⁶ F. Di Lodovico,³⁶ R. Sacco,³⁶ M. Sigamani,³⁶ G. Cowan,³⁷ D. N. Brown,³⁸ C. L. Davis,³⁸ A. G. Denig,³⁹ M. Fritsch,³⁹ W. Gradl,³⁹ K. Griessinger,³⁹ A. Hafner,³⁹ E. Prencipe,³⁹ R. J. Barlow,^{40,‡} G. D. Lafferty,⁴⁰ E. Behn,⁴¹ R. Cenci,⁴¹ B. Hamilton,⁴¹ A. Jawahery,⁴¹ D. A. Roberts,⁴¹ C. Dallapiccola,⁴² R. Cowan,⁴³ D. Dujmic,⁴³ G. Sciolla,⁴³ R. Cheaib,⁴⁴ P. M. Patel,^{44,§} S. H. Robertson,⁴⁴ P. Biassoni,^{45a,45b} N. Neri,^{45a} F. Palombo,^{45a,45b} L. Cremaldi,⁴⁶ R. Godang,^{46,||} R. Kroeger,⁴⁶ P. Sonnek,⁴⁶ D. J. Summers,⁴⁶ X. Nguyen,⁴⁷ M. Simard,⁴⁷ P. Taras,⁴⁷ G. De Nardo,^{48a,48b} D. Monorchio,^{48a,48b} G. Onorato,^{48a,48b} C. Sciacca,^{48a,48b} M. Martinelli,⁴⁹ G. Raven,⁴⁹ C. P. Jessop,⁵⁰ J. M. LoSecco,⁵⁰ K. Honscheid,⁵¹ R. Kass,⁵¹ J. Brau,⁵² R. Frey,⁵² N. B. Sinev,⁵² D. Strom,⁵² E. Torrence,⁵² E. Feltresi,^{53a,53b} N. Gagliardi,^{53a,53b} M. Margoni,^{53a,53b} M. Morandin,^{53a} M. Posocco,^{53a} M. Rotondo,^{53a} G. Simi,^{53a} F. Simonetto,^{53a,53b} R. Stroili,^{53a,53b} S. Akar,⁵⁴ E. Ben-Haim,⁵⁴ M. Bomben,⁵⁴ G. R. Bonneaud,⁵⁴ H. Briand,⁵⁴ G. Calderini,⁵⁴ J. Chauveau,⁵⁴ O. Hamon,⁵⁴ Ph. Leruste,⁵⁴ G. Marchiori,⁵⁴ J. Ocariz,⁵⁴ S. Sitt,⁵⁴ M. Biasini,^{55a,55b} E. Manoni,^{55a,55b} S. Pacetti,^{55a,55b} A. Rossi,^{55a,55b} C. Angelini,^{56a,56b} G. Batignani,^{56a,56b} S. Bettarini,^{56a,56b} M. Carpinelli,^{56a,56b,¶} G. Casarosa,^{56a,56b} A. Cervelli,^{56a,56b} F. Forti,^{56a,56b} M. A. Giorgi,^{56a,56b} A. Lusiani,^{56a,56c} B. Oberhof,^{56a,56b} E. Paoloni,^{56a,56b} A. Perez,^{56a} G. Rizzo,^{56a,56b} J. J. Walsh,^{56a} D. Lopes Pegna,⁵⁷ J. Olsen,⁵⁷ A. J. S. Smith,⁵⁷ F. Anulli,^{58a} R. Faccini,^{58a,58b} F. Ferrarotto,^{58a} F. Ferroni,^{58a,58b} M. Gaspero,^{58a,58b} L. Li Gioi,^{58a} M. A. Mazzoni,^{58a} G. Piredda,^{58a} C. B nger,⁵⁹ O. Gr nberg,⁵⁹ T. Hartmann,⁵⁹ T. Leddig,⁵⁹ C. Vo ,⁵⁹ R. Waldi,⁵⁹ T. Adye,⁶⁰ E. O. Olaiya,⁶⁰ F. F. Wilson,⁶⁰ S. Emery,⁶¹ G. Hamel de Monchenault,⁶¹ G. Vasseur,⁶¹ Ch. Y che,⁶¹ D. Aston,⁶² D. J. Bard,⁶² J. F. Benitez,⁶² C. Cartaro,⁶² M. R. Convery,⁶² J. Dorfan,⁶² G. P. Dubois-Felsmann,⁶² W. Dunwoodie,⁶² M. Ebert,⁶² R. C. Field,⁶² B. G. Fulsom,⁶² A. M. Gabareen,⁶² M. T. Graham,⁶² C. Hast,⁶² W. R. Innes,⁶² M. H. Kelsey,⁶² P. Kim,⁶² M. L. Kocian,⁶² D. W. G. S. Leith,⁶² P. Lewis,⁶² D. Lindemann,⁶² B. Lindquist,⁶² S. Luitz,⁶² V. Luth,⁶² H. L. Lynch,⁶² D. B. MacFarlane,⁶² D. R. Muller,⁶² H. Neal,⁶² S. Nelson,⁶² M. Perl,⁶² T. Pulliam,⁶² B. N. Ratcliff,⁶² A. Roodman,⁶² A. A. Salnikov,⁶² R. H. Schindler,⁶² A. Snyder,⁶² D. Su,⁶² M. K. Sullivan,⁶² J. Va'vra,⁶² A. P. Wagner,⁶² W. F. Wang,⁶² W. J. Wisniewski,⁶² M. Wittgen,⁶² D. H. Wright,⁶² H. W. Wulsin,⁶² V. Ziegler,⁶² W. Park,⁶³ M. V. Purohit,⁶³ R. M. White,⁶³ J. R. Wilson,⁶³ A. Randle-Conde,⁶⁴ S. J. Sekula,⁶⁴ M. Bellis,⁶⁵ P. R. Burchat,⁶⁵ T. S. Miyashita,⁶⁵ E. M. T. Puccio,⁶⁵ M. S. Alam,⁶⁶ J. A. Ernst,⁶⁶ R. Gorodeisky,⁶⁷ N. Guttman,⁶⁷ D. R. Peimer,⁶⁷ A. Soffer,⁶⁷ S. M. Spanier,⁶⁸ J. L. Ritchie,⁶⁹ A. M. Ruland,⁶⁹ R. F. Schwitters,⁶⁹ B. C. Wray,⁶⁹ J. M. Izen,⁷⁰ X. C. Lou,⁷⁰ F. Bianchi,^{71a,71b} D. Gamba,^{71a,71b} S. Zambito,^{71a,71b} L. Lanceri,^{72a,72b} L. Vitale,^{72a,72b} F. Martinez-Vidal,⁷³ A. Oyanguren,⁷³ P. Villanueva-Perez,⁷³ H. Ahmed,⁷⁴ J. Albert,⁷⁴ Sw. Banerjee,⁷⁴ F. U. Bernlochner,⁷⁴ H. H. F. Choi,⁷⁴ G. J. King,⁷⁴ R. Kowalewski,⁷⁴ M. J. Lewczuk,⁷⁴ I. M. Nugent,⁷⁴ J. M. Roney,⁷⁴ R. J. Sobie,⁷⁴

N. Tasneem,⁷⁴ T. J. Gershon,⁷⁵ P. F. Harrison,⁷⁵ T. E. Latham,⁷⁵ H. R. Band,⁷⁶ S. Dasu,⁷⁶ Y. Pan,⁷⁶
R. Prepost,⁷⁶ and S. L. Wu⁷⁶

(BABAR Collaboration)

- ¹*Laboratoire d'Annecy-le-Vieux de Physique des Particules (LAPP), Université de Savoie, CNRS/IN2P3, F-74941 Annecy-Le-Vieux, France*
²*Universitat de Barcelona, Facultat de Física, Departament ECM, E-08028 Barcelona, Spain*
^{3a}*INFN Sezione di Bari, I-70126 Bari, Italy*
^{3b}*Dipartimento di Fisica, Università di Bari, I-70126 Bari, Italy*
⁴*University of Bergen, Institute of Physics, N-5007 Bergen, Norway*
⁵*Lawrence Berkeley National Laboratory and University of California, Berkeley, California 94720, USA*
⁶*Ruhr Universität Bochum, Institut für Experimentalphysik I, D-44780 Bochum, Germany*
⁷*University of British Columbia, Vancouver, British Columbia, Canada V6T 1Z1*
⁸*Brunel University, Uxbridge, Middlesex UB8 3PH, United Kingdom*
⁹*Budker Institute of Nuclear Physics SB RAS, Novosibirsk 630090, Russia*
¹⁰*University of California at Irvine, Irvine, California 92697, USA*
¹¹*University of California at Riverside, Riverside, California 92521, USA*
¹²*University of California at Santa Barbara, Santa Barbara, California 93106, USA*
¹³*University of California at Santa Cruz, Institute for Particle Physics, Santa Cruz, California 95064, USA*
¹⁴*California Institute of Technology, Pasadena, California 91125, USA*
¹⁵*University of Cincinnati, Cincinnati, Ohio 45221, USA*
¹⁶*University of Colorado, Boulder, Colorado 80309, USA*
¹⁷*Colorado State University, Fort Collins, Colorado 80523, USA*
¹⁸*Technische Universität Dortmund, Fakultät Physik, D-44221 Dortmund, Germany*
¹⁹*Technische Universität Dresden, Institut für Kern- und Teilchenphysik, D-01062 Dresden, Germany*
²⁰*Laboratoire Leprince-Ringuet, Ecole Polytechnique, CNRS/IN2P3, F-91128 Palaiseau, France*
²¹*University of Edinburgh, Edinburgh EH9 3JZ, United Kingdom*
^{22a}*INFN Sezione di Ferrara, I-44100 Ferrara, Italy*
^{22b}*Dipartimento di Fisica, Università di Ferrara, I-44100 Ferrara, Italy*
²³*INFN Laboratori Nazionali di Frascati, I-00044 Frascati, Italy*
^{24a}*INFN Sezione di Genova, I-16146 Genova, Italy*
^{24b}*Dipartimento di Fisica, Università di Genova, I-16146 Genova, Italy*
²⁵*Indian Institute of Technology Guwahati, Guwahati, Assam 781 039, India*
²⁶*Harvard University, Cambridge, Massachusetts 02138, USA*
²⁷*Universität Heidelberg, Physikalisches Institut, Philosophenweg 12, D-69120 Heidelberg, Germany*
²⁸*Humboldt-Universität zu Berlin, Institut für Physik, Newtonstrasse 15, D-12489 Berlin, Germany*
²⁹*Imperial College London, London, SW7 2AZ, United Kingdom*
³⁰*University of Iowa, Iowa City, Iowa 52242, USA*
³¹*Iowa State University, Ames, Iowa 50011-3160, USA*
³²*Johns Hopkins University, Baltimore, Maryland 21218, USA*
³³*Laboratoire de l'Accélérateur Linéaire, IN2P3/CNRS et Université Paris-Sud 11, Centre Scientifique d'Orsay, B. P. 34, F-91898 Orsay Cedex, France*
³⁴*Lawrence Livermore National Laboratory, Livermore, California 94550, USA*
³⁵*University of Liverpool, Liverpool L69 7ZE, United Kingdom*
³⁶*Queen Mary, University of London, London E1 4NS, United Kingdom*
³⁷*University of London, Royal Holloway and Bedford New College, Egham, Surrey TW20 0EX, United Kingdom*
³⁸*University of Louisville, Louisville, Kentucky 40292, USA*
³⁹*Johannes Gutenberg-Universität Mainz, Institut für Kernphysik, D-55099 Mainz, Germany*
⁴⁰*University of Manchester, Manchester M13 9PL, United Kingdom*
⁴¹*University of Maryland, College Park, Maryland 20742, USA*
⁴²*University of Massachusetts, Amherst, Massachusetts 01003, USA*
⁴³*Massachusetts Institute of Technology, Laboratory for Nuclear Science, Cambridge, Massachusetts 02139, USA*
⁴⁴*McGill University, Montréal, Québec, Canada H3A 2T8*
^{45a}*INFN Sezione di Milano, I-20133 Milano, Italy*
^{45b}*Dipartimento di Fisica, Università di Milano, I-20133 Milano, Italy*
⁴⁶*University of Mississippi, University, Mississippi 38677, USA*
⁴⁷*Université de Montréal, Physique des Particules, Montréal, Québec, Canada H3C 3J7*
^{48a}*INFN Sezione di Napoli, I-80126 Napoli, Italy*
^{48b}*Dipartimento di Scienze Fisiche, Università di Napoli Federico II, I-80126 Napoli, Italy*

⁴⁹NIKHEF, National Institute for Nuclear Physics and High Energy Physics, NL-1009 DB Amsterdam, The Netherlands

⁵⁰University of Notre Dame, Notre Dame, Indiana 46556, USA

⁵¹Ohio State University, Columbus, Ohio 43210, USA

⁵²University of Oregon, Eugene, Oregon 97403, USA

^{53a}INFN Sezione di Padova, I-35131 Padova, Italy

^{53b}Dipartimento di Fisica, Università di Padova, I-35131 Padova, Italy

⁵⁴Laboratoire de Physique Nucléaire et de Hautes Energies, IN2P3/CNRS, Université Pierre et Marie Curie-Paris6, Université Denis Diderot-Paris7, F-75252 Paris, France

^{55a}INFN Sezione di Perugia, I-06100 Perugia, Italy

^{55b}Dipartimento di Fisica, Università di Perugia, I-06100 Perugia, Italy

^{56a}INFN Sezione di Pisa, I-56127 Pisa, Italy

^{56b}Dipartimento di Fisica, Università di Pisa, I-56127 Pisa, Italy

^{56c}Scuola Normale Superiore di Pisa, I-56127 Pisa, Italy

⁵⁷Princeton University, Princeton, New Jersey 08544, USA

^{58a}INFN Sezione di Roma, I-00185 Roma, Italy

^{58b}Dipartimento di Fisica, Università di Roma La Sapienza, I-00185 Roma, Italy

⁵⁹Universität Rostock, D-18051 Rostock, Germany

⁶⁰Rutherford Appleton Laboratory, Chilton, Didcot, Oxon, OX11 0QX, United Kingdom

⁶¹CEA, Irfu, SPP, Centre de Saclay, F-91191 Gif-sur-Yvette, France

⁶²SLAC National Accelerator Laboratory, Stanford, California 94309 USA

⁶³University of South Carolina, Columbia, South Carolina 29208, USA

⁶⁴Southern Methodist University, Dallas, Texas 75275, USA

⁶⁵Stanford University, Stanford, California 94305-4060, USA

⁶⁶State University of New York, Albany, New York 12222, USA

⁶⁷Tel Aviv University, School of Physics and Astronomy, Tel Aviv, 69978, Israel

⁶⁸University of Tennessee, Knoxville, Tennessee 37996, USA

⁶⁹University of Texas at Austin, Austin, Texas 78712, USA

⁷⁰University of Texas at Dallas, Richardson, Texas 75083, USA

^{71a}INFN Sezione di Torino, I-10125 Torino, Italy

^{71b}Dipartimento di Fisica Sperimentale, Università di Torino, I-10125 Torino, Italy

^{72a}INFN Sezione di Trieste, I-34127 Trieste, Italy

^{72b}Dipartimento di Fisica, Università di Trieste, I-34127 Trieste, Italy

⁷³IFIC, Universitat de Valencia-CSIC, E-46071 Valencia, Spain

⁷⁴University of Victoria, Victoria, British Columbia, Canada V8W 3P6

⁷⁵Department of Physics, University of Warwick, Coventry CV4 7AL, United Kingdom

⁷⁶University of Wisconsin, Madison, Wisconsin 53706, USA

(Received 3 February 2013; published 10 May 2013)

The process $e^+e^- \rightarrow p\bar{p}\gamma$ is studied using 469 fb^{-1} of integrated luminosity collected with the BABAR detector at the SLAC National Accelerator Laboratory, at an e^+e^- center-of-mass energy of 10.6 GeV. From the analysis of the $p\bar{p}$ invariant mass spectrum, the energy dependence of the cross section for $e^+e^- \rightarrow p\bar{p}$ is measured from threshold to 4.5 GeV. The energy dependence of the ratio of electric and magnetic form factors, $|G_E/G_M|$, and the asymmetry in the proton angular distribution are measured for $p\bar{p}$ masses below 3 GeV. The branching fractions for the decays $J/\psi \rightarrow p\bar{p}$ and $\psi(2S) \rightarrow p\bar{p}$ are also determined.

DOI: [10.1103/PhysRevD.87.092005](https://doi.org/10.1103/PhysRevD.87.092005)

PACS numbers: 13.66.Bc, 13.25.Gv, 13.40.Gp, 14.20.Dh

I. INTRODUCTION

In this paper we use the initial-state-radiation (ISR) technique to study the $e^+e^- \rightarrow p\bar{p}$ process over a wide range of center-of-mass (c.m.) energies. The study is an update of the results in Ref. [1], using a data sample that is about twice as large and improved analysis techniques. The Born cross section for the ISR process $e^+e^- \rightarrow p\bar{p}\gamma$ integrated over the nucleon momenta is

*Now at the University of Tabuk, Tabuk 71491, Saudi Arabia.

†Also with Università di Perugia, Dipartimento di Fisica, Perugia, Italy.

‡Now at the University of Huddersfield, Huddersfield HD1 3DH, UK.

§Deceased.

||Now at University of South Alabama, Mobile, Alabama 36688, USA.

¶Also with Università di Sassari, Sassari, Italy.

$$\frac{d^2\sigma_{e^+e^- \rightarrow p\bar{p}\gamma}(M_{p\bar{p}})}{dM_{p\bar{p}}d\cos\theta_\gamma^*} = \frac{2M_{p\bar{p}}}{s} W(s, x, \theta_\gamma^*) \sigma_{p\bar{p}}(M_{p\bar{p}}), \quad (1)$$

where $\sigma_{p\bar{p}}(m)$ is the Born cross section for the nonradiative process $e^+e^- \rightarrow p\bar{p}$, $M_{p\bar{p}}$ is the $p\bar{p}$ invariant mass, \sqrt{s} is the nominal e^+e^- c.m. energy, $x \equiv 2E_\gamma^*/\sqrt{s} = 1 - M_{p\bar{p}}^2/s$, and E_γ^* and θ_γ^* are the ISR photon energy and polar angle, respectively, in the e^+e^- c.m. frame.¹ The function $W(s, x, \theta_\gamma^*)$ [2] describes the probability of ISR photon emission. The Born cross section for $e^+e^- \rightarrow p\bar{p}$ is

$$\sigma_{p\bar{p}}(M_{p\bar{p}}) = \frac{4\pi\alpha^2\beta C}{3M_{p\bar{p}}^2} \left[|G_M(M_{p\bar{p}})|^2 + \frac{2m_p^2}{M_{p\bar{p}}^2} |G_E(M_{p\bar{p}})|^2 \right], \quad (2)$$

where m_p is the nominal proton mass, $\beta = \sqrt{1 - 4m_p^2/M_{p\bar{p}}^2}$, $C = y/(1 - e^{-y})$ with $y = \pi\alpha/\beta$ is the Coulomb correction factor (see Ref. [3] and references therein), which results in a nonzero cross section at threshold, and G_M and G_E are the magnetic and electric form factors, respectively ($|G_E| = |G_M|$ at threshold). From measurement of the cross section, a linear combination of the squared form factors can be determined. We define the effective form factor

$$|F_p(M_{p\bar{p}})| = \sqrt{\frac{|G_M(M_{p\bar{p}})|^2 + 2m_p^2/M_{p\bar{p}}^2 |G_E(M_{p\bar{p}})|^2}{1 + 2m_p^2/M_{p\bar{p}}^2}}, \quad (3)$$

which is proportional to the square root of the measured $e^+e^- \rightarrow p\bar{p}$ cross section.

The proton angular distribution in $e^+e^- \rightarrow p\bar{p}\gamma$ [4] can be expressed as a sum of terms proportional to $|G_M|^2$ and $|G_E|^2$. The angular dependences of the G_M and G_E terms are approximately $1 + \cos^2\theta_p$ and $\sin^2\theta_p$, respectively, where θ_p is the angle between the proton momentum in the $p\bar{p}$ rest frame and the momentum of the $p\bar{p}$ system in the e^+e^- c.m. frame. Thus, the study of the proton angular distribution can be used to determine the modulus of the ratio of the electric and magnetic form factors.

Direct measurements of the $e^+e^- \rightarrow p\bar{p}$ cross section are available from e^+e^- experiments [5–11]. Most of these results assume $|G_E| = |G_M|$. The proton form factor was also determined in the inverse reaction $p\bar{p} \rightarrow e^+e^-$ [12–14]. In the PS170 experiment [12] at LEAR, this reaction was studied in the c.m. energy range from threshold up to 2.05 GeV. A strong dependence of the form factor on c.m. energy near threshold was observed. The $|G_E/G_M|$ ratio was found to be consistent with unity. The E760 [13] and E835 [14] experiments at Fermilab observed a strong decrease of the form factor for

c.m. energies above 3 GeV, in agreement with expectation $\alpha_s^2(m^2)/m^4$ from perturbative QCD. However, a recent result [11] based on e^+e^- data indicates that the decrease of the form factor above 4 GeV is somewhat more gradual.

II. THE BABAR DETECTOR AND EVENT SAMPLES

The data, corresponding to an integrated luminosity of 469 fb⁻¹, were recorded with the BABAR detector at the SLAC PEP-II asymmetric-energy e^+e^- collider. About 90% of the data were collected at a c.m. energy of 10.58 GeV, near the maximum of $Y(4S)$ resonance, while 10% were recoded at 10.54 GeV.

The BABAR detector is described in detail elsewhere [15]. Charged-particle momenta are measured by a combination of a five-layer silicon vertex tracker and a 40-layer drift chamber (DCH) operating in a 1.5-T solenoidal magnetic field. Charged-particle identification (PID) is based on energy-loss measurements in the silicon vertex tracker and DCH, and information from a ring-imaging Cherenkov detector. Photons and electrons are detected in a CsI(Tl) electromagnetic calorimeter. Muons are identified by resistive-plate chambers or streamer tubes [16] in the instrumented magnetic flux return.

Simulated events for signal and background ISR processes are obtained with event generators based on Ref. [17]. The differential cross section for $e^+e^- \rightarrow p\bar{p}\gamma$ is taken from Ref. [4]. To analyze the experimental proton angular distribution, two samples of signal events are generated, one with $G_E = 0$ and the other with $G_M = 0$. Since the polar-angle distribution of the ISR photon is peaked along the beam axis, the MC events are generated with the restriction $20^\circ < \theta_\gamma^* < 160^\circ$ (the corresponding angular range in the laboratory frame is $12^\circ < \theta_\gamma < 146^\circ$). Additional photon radiation from the initial state is generated by the structure function method [18]. To restrict the maximum energy of the extra photons, the invariant mass of the hadron system and the ISR photon is required to be greater than 8 GeV/ c^2 . For background $e^+e^- \rightarrow \mu^+\mu^-\gamma$, $\pi^+\pi^-\gamma$, and $K^+K^-\gamma$ processes, final-state radiation is generated using the PHOTOS package [19]. Background from $e^+e^- \rightarrow q\bar{q}$ is simulated with the JETSET [20] event generator; JETSET also generates ISR events with a hadron invariant mass above 2 GeV/ c^2 , and therefore can be used to study the ISR background with baryons in the final state. The dominant background process, $e^+e^- \rightarrow p\bar{p}\pi^0$, is simulated separately. Its angular and energy distributions are generated according to three-body phase space.

The detector response is simulated using the GEANT4 [21] package. The simulation takes into account the variations in the detector and beam background conditions over the running period of the experiment.

¹Throughout this paper, the asterisk denotes quantities in the e^+e^- center-of-mass frame. All other variables except θ_p are defined in the laboratory frame.

III. EVENT SELECTION

The preliminary selection of $e^+e^- \rightarrow p\bar{p}\gamma$ candidates requires that all of the final-state particles be detected and well reconstructed. Events are selected with at least two tracks with opposite charge and a photon candidate with $E_\gamma^* > 3$ GeV and polar angle in the range $20^\circ < \theta_\gamma < 137.5^\circ$. Each charged-particle track must extrapolate to the interaction region, have transverse momentum greater than 0.1 GeV/c, have a polar angle in the range $25.8^\circ < \theta < 137.5^\circ$, and be identified as a proton. Since a significant fraction of the events contains beam-generated background photons and charged tracks, any number of extra tracks and photons is allowed in an event.

The expected number of events from the background processes $e^+e^- \rightarrow \pi^+\pi^-\gamma$, $\mu^+\mu^-\gamma$, and $K^+K^-\gamma$ exceeds the number of signal events by 2 to 3 orders of magnitude. These backgrounds are significantly suppressed by the requirement that both charged particles be identified as protons. The suppression is a factor of 3×10^4 for pion and muon events, and a factor 10^4 for kaon events, with a loss of approximately 30% of the signal events.

Further background suppression is based on kinematic fitting. We perform a kinematic fit to the $e^+e^- \rightarrow h^+h^-\gamma$ hypothesis with requirements of energy and momentum conservation. Here h can be π , K , or p , and γ refers to the photon with highest c.m. energy. In the case of events with more than two charged tracks, the fit uses the parameters of the two oppositely charged tracks that have the minimum distance from the interaction point in the azimuthal plane. Two conditions on the χ^2 of the kinematic fits are used: $\chi_p^2 < 30$ and $\chi_K^2 > 30$, where χ_p^2 and χ_K^2 are the χ^2 values for the proton and kaon mass hypotheses, respectively. The χ_p^2 distribution for simulated $p\bar{p}\gamma$ events is shown in Fig. 1. The tail at high χ^2 is due to events with extra soft

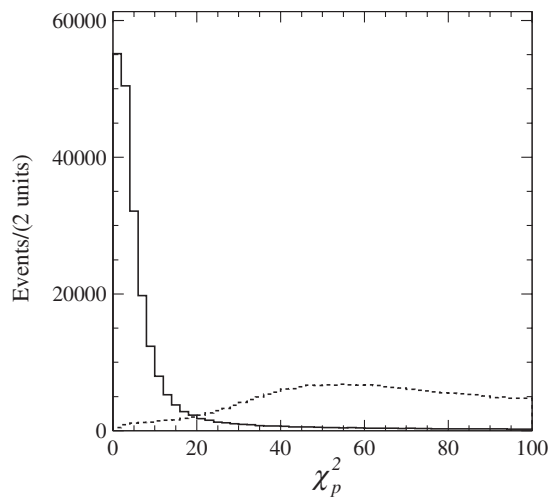


FIG. 1. The χ_p^2 distribution for simulated $e^+e^- \rightarrow p\bar{p}\gamma$ (solid histogram) and $e^+e^- \rightarrow K^+K^-\gamma$ (dashed histogram, arbitrary normalization) events.

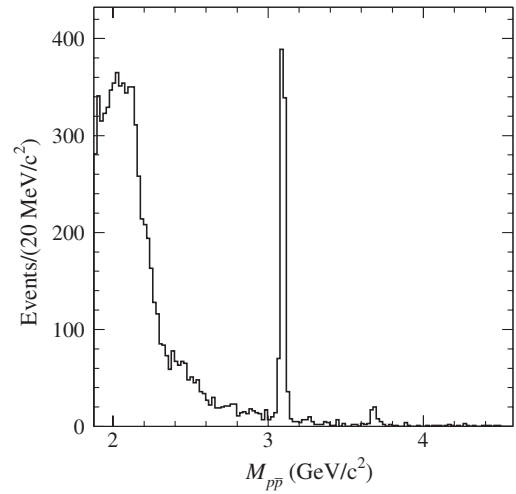


FIG. 2. The $p\bar{p}$ invariant mass spectrum for the selected data $p\bar{p}\gamma$ candidates. The left edge of the plot corresponds to the $p\bar{p}$ threshold.

photons emitted in the initial state. The dashed histogram represents the χ_p^2 distribution for $K^+K^-\gamma$ simulated events. The χ^2 requirements provide additional background suppression by a factor of 50 for pion and muon events, and a factor of 30 for kaon events, with a loss of 25% of the signal events.

The $p\bar{p}$ invariant mass distribution is shown in Fig. 2 for the 8298 selected data events. Most of the events have $p\bar{p}$ mass less than 3 GeV/c². Signals from $J/\psi \rightarrow p\bar{p}$ and $\psi(2S) \rightarrow p\bar{p}$ decays are clearly seen.

IV. BACKGROUND EVALUATION

Potential sources of background in the sample of selected $e^+e^- \rightarrow p\bar{p}\gamma$ candidates are the processes $e^+e^- \rightarrow \pi^+\pi^-\gamma$, $e^+e^- \rightarrow K^+K^-\gamma$, $e^+e^- \rightarrow \mu^+\mu^-\gamma$, and $e^+e^- \rightarrow e^+e^-\gamma$, in which the charged particles are misidentified as protons, and processes with protons and neutral particle(s) in the final state, such as $e^+e^- \rightarrow p\bar{p}\pi^0$, $p\bar{p}\pi^0\gamma$.

The contribution of final-state radiation to the total cross section for the process $e^+e^- \rightarrow p\bar{p}\gamma$ in the mass region of interest (below 4.5 GeV) was estimated in Ref. [1] and found to be negligible (about 10^{-3} of the ISR cross section).

A. Background contributions from $e^+e^- \rightarrow \pi^+\pi^-\gamma$, $e^+e^- \rightarrow K^+K^-\gamma$, $e^+e^- \rightarrow e^+e^-\gamma$, and $e^+e^- \rightarrow \mu^+\mu^-\gamma$

The background contribution from $e^+e^- \rightarrow \pi^+\pi^-\gamma$ is estimated using Monte Carlo (MC) simulation. To study how the simulation reproduces misidentification probability for pions, special pion-enriched data samples are

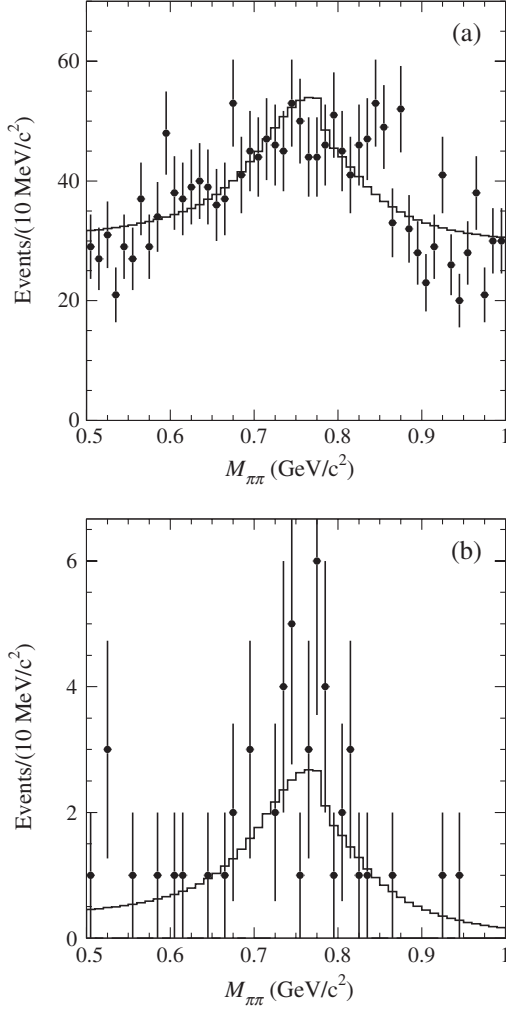


FIG. 3. (a) The $M_{\pi\pi}$ spectrum for data events with $\chi_p^2 < 30$ and $\chi_K^2 > 30$, and one proton candidate (selection 2 in the text); (b) the same spectrum for data events with $\chi_\pi^2 < 20$ and two proton candidates (selection 3 in the text). The histograms are the results of the fit described in the text.

selected with the following requirements on PID and on the χ^2 of the kinematic fits:

- (1) one proton candidate, $\chi_\pi^2 < 20$;
- (2) one proton candidate, $\chi_p^2 < 30$, $\chi_K^2 > 30$;
- (3) two proton candidates, $\chi_\pi^2 < 20$.

Here χ_π^2 is the χ^2 for the pion mass hypothesis.

The distributions of the invariant mass calculated under the pion-mass hypothesis ($M_{\pi\pi}$) for data events selected with criteria 2 and 3 are shown in Fig. 3. The spectra are fit with a sum of the mass spectra for simulated $\pi^+\pi^-\gamma$ events (ρ -meson line shape with ω - ρ interference) and a linear background term. The numbers of $\pi\pi\gamma$ events with $0.5 < M_{\pi\pi} < 1$ GeV/ c^2 obtained from the fits for selections 1–3 are listed in Table I, together with the corresponding numbers of events expected from the $\pi^+\pi^-\gamma$ MC simulation.

Since the simulation correctly predicts the numbers of pion events for selections 1–3, we use it to estimate the

TABLE I. The numbers of $\pi\pi\gamma$ events for data and MC simulation with $0.5 < M_{\pi\pi} < 1$ GeV/ c^2 that satisfy different selection criteria for data and MC simulation. The data numbers are obtained from the fits to the $M_{\pi\pi}$ distributions described in the text.

Selection	Data	MC simulation
1	15310 ± 160	14800 ± 180
2	400 ± 60	460 ± 30
3	41 ± 8	48 ± 11

pion background for our standard selection. We observe no events satisfying the standard selection criteria in the $\pi\pi\gamma$ MC sample. The corresponding upper limit on the $\pi\pi\gamma$ background in the data sample is 5.2 events at 90% confidence level (C.L.). The estimated pion background is less than 0.1% of the number of selected $p\bar{p}\gamma$ candidates.

Similarly, the number of $e^+e^- \rightarrow K^+K^-\gamma$ events can be estimated from the number of events in the ϕ meson peak in the distribution of invariant mass of the charged particles calculated under the kaon hypothesis. It is found that the $K^+K^-\gamma$ MC simulation predicts reasonably well the numbers of kaon events in the data sample with one identified kaon and the standard χ^2 conditions, and in the data sample with two identified kaons and $\chi_K^2 < 20$. Therefore we use the MC simulation to estimate the kaon background for the standard selection. The estimated background, 1.6 ± 0.8 events, is significantly less than 0.1% of the number of data events selected.

The specific kinematic properties of the $e^+e^- \rightarrow e^+e^-\gamma$ process are used to estimate the electron background. In a significant fraction (about 50%) of detected $e^+e^-\gamma$ events the photon is emitted along the final electron direction. These events have e^+e^- invariant mass in the range from 3 to 7 GeV/ c^2 and can be selected by the requirement $\cos\psi^* < -0.98$, where ψ^* is the angle between the two charged tracks in the initial e^+e^- c.m. frame. In the sample of selected $p\bar{p}\gamma$ candidates we observe no events having the above characteristics. The corresponding 90% C.L. upper limit on the $e^+e^-\gamma$ background in the data sample is 4.6 events (2 events with $M_{p\bar{p}} < 4.5$ GeV/ c^2).

To compare MC simulation and data for the process $e^+e^- \rightarrow \mu^+\mu^-\gamma$, we use a subsample of events selected with the requirement that both charged particles be identified as muons. Muon identification is based on instrumented magnetic flux return information, and does not use ring-imaging Cherenkov detector or dE/dx information, which are necessary for proton identification. In the data samples with one or two identified protons obtained with the standard χ^2 selection, we select 86 and 2 muon-identified events, respectively. These numbers can be compared with 60 ± 16 and zero events expected from the $e^+e^- \rightarrow \mu^+\mu^-\gamma$ simulation. Taking into account that the ratio of the total number of $\mu^+\mu^-\gamma$ events to those with two identified muons is about two to one, we estimate

the $\mu^+\mu^-\gamma$ background for the standard selection criteria to be 4.0 ± 2.8 events.

The combined background from the processes $e^+e^- \rightarrow h^+h^-\gamma$, $h = \pi, K, e, \mu$ is less than 0.2% of the number of selected $p\bar{p}\gamma$ candidates, and so can be neglected.

B. Background from $e^+e^- \rightarrow p\bar{p}\pi^0$

The main source of background for the process under study is $e^+e^- \rightarrow p\bar{p}\pi^0$. The $p\bar{p}\pi^0$ events with an undetected low-energy photon, or with merged photons from the π^0 decay, are kinematically reconstructed with a low χ_p^2 value and so cannot be separated from the signal process. This background is studied by selecting a special subsample of data events containing two charged particles identified as protons and at least two photons with energy greater than 0.1 GeV, one of which must have c.m. energy above 3 GeV. The two-photon invariant mass $M_{\gamma\gamma}$ is required to be in the range 0.07–0.20 GeV/ c^2 , which is centered on the nominal π^0 mass. A kinematic fit to the $e^+e^- \rightarrow p\bar{p}\gamma\gamma$ hypothesis is then performed. Conditions on the χ^2 of the kinematic fit ($\chi^2 < 25$) and the two-photon invariant mass ($0.1025 < M_{\gamma\gamma} < 0.1675$ GeV/ c^2) are imposed in order to select $e^+e^- \rightarrow p\bar{p}\pi^0$ candidates. Possible background is estimated using the $M_{\gamma\gamma}$ sidebands $0.0700 < M_{\gamma\gamma} < 0.1025$ GeV/ c^2 and $0.1675 < M_{\gamma\gamma} < 0.2000$ GeV/ c^2 . The $M_{p\bar{p}}$ spectra and $\cos\theta_p$ distributions for data events from the signal and sideband $M_{\gamma\gamma}$ regions are shown in Fig. 4. The total number of selected events is 148 in the signal region and 12 in the sidebands. The expected number of $e^+e^- \rightarrow p\bar{p}\pi^0$ events in the $M_{\gamma\gamma}$ sidebands is 5.4.

To study the $e^+e^- \rightarrow p\bar{p}\pi^0$ background, the sample of simulated $e^+e^- \rightarrow p\bar{p}\pi^0$ events is generated according to three-body phase space, but with an additional weight proportional to $(M_{p\bar{p}} - 2m_p)^{3/2}$ to imitate the $M_{p\bar{p}}$ distribution observed in data. The simulation well reproduces the observed $\cos\theta_p$ distribution.

In Fig. 5 the $\cos\theta_\pi^*$ distribution for selected data and simulated $e^+e^- \rightarrow p\bar{p}\pi^0$ events is shown, where θ_π^* is the π^0 polar angle in the e^+e^- c.m. frame. It is seen that the data and simulated distributions differ slightly. Since we do not observe a significant variation of the $\cos\theta_\pi^*$ distribution with $M_{p\bar{p}}$ in data, we use the data distribution averaged over $M_{p\bar{p}}$ (Fig. 5) to reweight the $e^+e^- \rightarrow p\bar{p}\pi^0$ simulation.

From the reweighted simulation, we calculate the ratio (K_{MC}) of the $M_{p\bar{p}}$ distribution for events selected with the standard $p\bar{p}\gamma$ criteria to that selected with the $p\bar{p}\pi^0$ criteria. The value of the ratio K_{MC} varies from 3.4 near $p\bar{p}$ threshold to 2.0 at 5 GeV/ c^2 . The expected $M_{p\bar{p}}$ spectrum for the $e^+e^- \rightarrow p\bar{p}\pi^0$ background events satisfying the $p\bar{p}\gamma$ selection criteria is evaluated as $K_{MC}(M_{p\bar{p}}) \times (dN/dM_{p\bar{p}})_{\text{data}}$, where $(dN/dM_{p\bar{p}})_{\text{data}}$ is the mass distribution for $e^+e^- \rightarrow p\bar{p}\pi^0$ events obtained above [Fig. 4(a)].

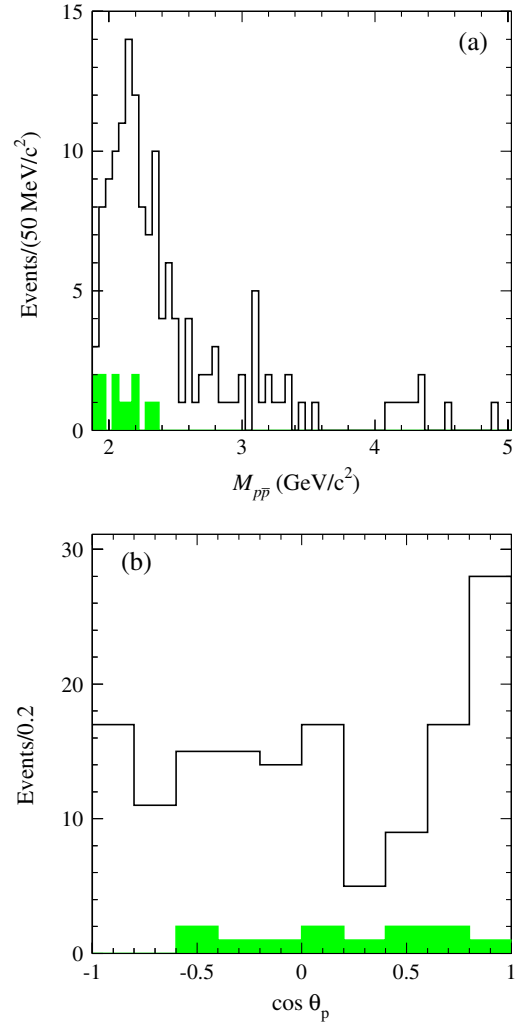


FIG. 4 (color online). (a) The $M_{p\bar{p}}$ spectrum and (b) the $\cos\theta_p$ distribution for selected $e^+e^- \rightarrow p\bar{p}\pi^0$ candidates in data. In each figure, the shaded histogram shows the background contribution estimated from the $M_{\gamma\gamma}$ sidebands.

The spectrum is shown in Fig. 6. The number of selected $e^+e^- \rightarrow p\bar{p}\gamma$ candidates and the expected number of $e^+e^- \rightarrow p\bar{p}\pi^0$ background events are given for different $p\bar{p}$ mass ranges in Table II. The background increases from 5% near $p\bar{p}$ threshold to 50% at $M_{p\bar{p}} \approx 4$ GeV/ c^2 . Above 4.5 GeV/ c^2 , the number of observed $p\bar{p}\gamma$ candidates is consistent with expected $p\bar{p}\pi^0$ background.

C. Other sources of background

Other possible background sources are ISR processes with higher final-state multiplicity ($e^+e^- \rightarrow p\bar{p}\pi^0\gamma, p\bar{p}2\pi^0\gamma, \dots$), and direct e^+e^- annihilation processes other than $e^+e^- \rightarrow p\bar{p}\pi^0$ ($e^+e^- \rightarrow p\bar{p}\eta, e^+e^- \rightarrow p\bar{p}2\pi^0, \dots$). All of these processes are simulated by JETSET, which predicts the ISR background to be 55 ± 6 events and the direct annihilation background to be 40 ± 5 events. The total predicted background from these two

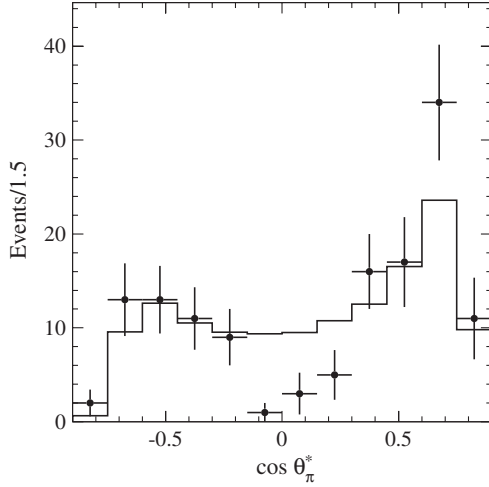


FIG. 5. The $\cos \theta_\pi^*$ distribution for $e^+e^- \rightarrow p\bar{p}\pi^0$ event candidates for data (points with error bars) and simulation (histogram).

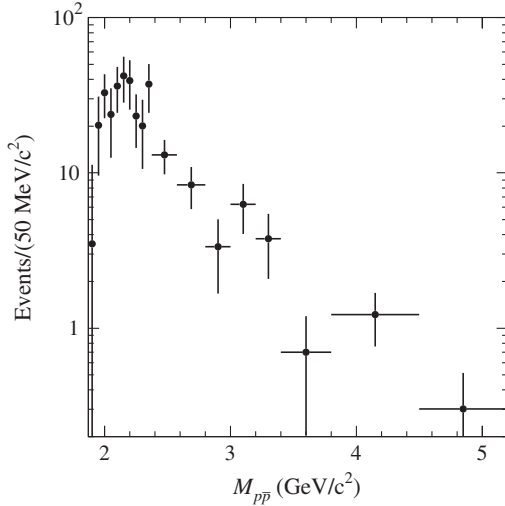


FIG. 6. The expected $M_{p\bar{p}}$ spectrum for $e^+e^- \rightarrow p\bar{p}\pi^0$ events selected with the standard $p\bar{p}\gamma$ criteria. The spectrum is obtained by scaling the data distribution shown in Fig. 4(a) by the factor $K_{MC}(M_{p\bar{p}})$ described in the text.

sources is about 1.2% of the number of selected $p\bar{p}\gamma$ candidates. We do not perform a detailed study of these background processes. Their contribution is estimated from data by using the χ^2 sideband region, as described below in Sec. IV D.

TABLE II. The number of selected $p\bar{p}\gamma$ candidates, $N_{p\bar{p}\gamma}$, and the number of background events from the $e^+e^- \rightarrow p\bar{p}\pi^0$ process, $N_{p\bar{p}\pi^0}$, for different ranges of $M_{p\bar{p}}$. The $p\bar{p}$ mass ranges near the J/ψ and $\psi(2S)$ resonances are excluded.

$M_{p\bar{p}}$ (GeV/ c^2)	<2.50	2.50–3.05	3.15–3.60	3.75–4.50	>4.5
$N_{p\bar{p}\gamma}$	6695	592	76	29	9
$N_{p\bar{p}\pi^0}$	321 ± 37	66 ± 15	26 ± 9	17 ± 6	6 ± 3

TABLE III. The number of selected $p\bar{p}\gamma$ candidates from the mass region $M_{p\bar{p}} < 4.5$ GeV/ c^2 with $\chi_p^2 < 30$ (N_1) and $30 < \chi_p^2 < 60$ (N_2) for signal and for different background processes; β_i is the ratio N_2/N_1 obtained from simulation. The first column shows the numbers of $p\bar{p}\gamma$ candidates selected in data. The numbers for $e^+e^- \rightarrow p\bar{p}\gamma$ are obtained from data using the background subtraction procedure described in the text.

	Data	$p\bar{p}\pi^0$	e^+e^-	Other ISR	$p\bar{p}\gamma$
N_1	8298	448 ± 42	40 ± 5	55 ± 6	7741 ± 113
N_2	560	79 ± 7	76 ± 7	74 ± 7	337 ± 16
β_i		0.175 ± 0.04	1.88 ± 0.29	1.34 ± 0.18	0.0435 ± 0.0020

D. Background subtraction

The expected number of background events estimated in the previous sections is summarized in Table III. The “Other ISR” and “ e^+e^- ” columns show the background contributions estimated with JETSET that result from ISR processes and from e^+e^- annihilation processes other than $e^+e^- \rightarrow p\bar{p}\pi^0$. Because JETSET has not been precisely validated for the rare processes contributing to the $p\bar{p}\gamma$ candidate sample, we use a method of background estimation that is based on the difference in χ^2 distributions between signal and background events. The first and second rows in Table III show the expected numbers of signal and background events with $\chi_p^2 < 30$ (N_1) and $30 < \chi_p^2 < 60$ (N_2). The last row lists the ratio $\beta_i = N_2/N_1$.

The coefficients β_i for signal events and for background events from the “ e^+e^- ” and “Other ISR” columns are very different. This difference is used to estimate and subtract the background from these two sources. The numbers of signal and background (from “ e^+e^- ” and “ISR” sources) events with $\chi_p^2 < 30$ can be calculated as

$$N_{\text{sig}} = \frac{N'_1 - N'_2/\beta_{\text{bkg}}}{1 - \beta_{p\bar{p}\gamma}/\beta_{\text{bkg}}}, \quad N_{\text{bkg}} = N'_1 - N_{\text{sig}}, \quad (4)$$

where N'_1 and N'_2 are the numbers of data events in the signal and sideband χ^2 regions after subtraction of the $p\bar{p}\pi^0$ background, and β_{bkg} is the N_2/N_1 ratio averaged over all background processes of the e^+e^- and ISR types. For this coefficient, $\beta_{\text{bkg}} = 1.6 \pm 0.3$ is used; it is the average of $\beta_{e^+e^-}$ and β_{ISR} with the uncertainty $(\beta_{e^+e^-} - \beta_{\text{ISR}})/2$. The $\beta_{p\bar{p}\gamma}$ coefficient is determined from signal simulation and corrected for the data-simulation difference in the χ^2 distribution. The data-simulation difference is studied using $e^+e^- \rightarrow \mu^+\mu^-\gamma$ events, which are very similar kinematically to the signal events and can be selected with negligible background. The ratio of the β coefficients for $e^+e^- \rightarrow \mu^+\mu^-\gamma$ data and simulation is independent of the $\mu^+\mu^-$ mass and is equal to 1.008 ± 0.008 . The corrected $\beta_{p\bar{p}\gamma}$ value varies from 0.043 at $p\bar{p}$ threshold to 0.048 at 4.5 GeV/ c^2 .

The total numbers of $e^+e^- \rightarrow p\bar{p}\gamma$ events (N_{sig}) and background events from e^+e^- and ISR sources (N_{bkg}) in

the signal region are found to be $7741 \pm 95 \pm 62$ and $109 \pm 16 \pm 25$, respectively. The systematic uncertainty on N_{sig} is dominated by the uncertainty in the $p\bar{p}\pi^0$ background. The number of background events is in good agreement with the estimate from simulation, $(40 \pm 5) + (55 \pm 6) = 95 \pm 8$. The total background in the signal χ_p^2 region is 531 ± 51 events, which is about 7% of the number of signal events.

The background subtraction procedure is performed in each $p\bar{p}$ mass interval. The number of selected events for each interval after background subtraction and correction for event migration between intervals (see Sec. VII) is listed in Table VI below. The events from J/ψ and $\psi(2S)$ decays are subtracted from the contents of the corresponding intervals.

V. ANGULAR DISTRIBUTIONS

The modulus of the ratio of the electric and magnetic form factors can be extracted from an analysis of the distribution of θ_p , the angle between the proton momentum in the $p\bar{p}$ rest frame, and the momentum of the $p\bar{p}$ system in the e^+e^- c.m. frame. This distribution is given by

$$\frac{dN}{d\cos\theta_p} = A \left(H_M(\cos\theta_p, M_{p\bar{p}}) + \left| \frac{G_E}{G_M} \right|^2 H_E(\cos\theta_p, M_{p\bar{p}}) \right). \quad (5)$$

The angular dependences of the functions $H_M(\cos\theta_p, M_{p\bar{p}})$ and $H_E(\cos\theta_p, M_{p\bar{p}})$ are approximately $1 + \cos^2\theta_p$ and $\sin^2\theta_p$, almost independent of $p\bar{p}$ invariant mass, while their relative normalization strongly depends on mass, mainly due to the factor $2m_p^2/M_{p\bar{p}}^2$ contained in the G_E term [see Eq. (2)].

The angular distributions are studied in six intervals of $p\bar{p}$ invariant mass from threshold to 3 GeV/ c^2 . The mass intervals, the corresponding numbers of selected events, and the estimated numbers of background events are listed in Table IV. The angular distributions are shown in Fig. 7. The background is subtracted in each angular bin using the

TABLE IV. The number of selected $p\bar{p}\gamma$ candidates (N) and the number of background events (N_{bkg}) for each $p\bar{p}$ mass interval; $|G_E/G_M|$ is the fitted ratio of form factors.

$M_{p\bar{p}}, \text{GeV}/c^2$	N	N_{bkg}	$ G_E/G_M $
1.877–1.950	1162	19 ± 10	$1.36^{+0.15+0.05}_{-0.14-0.04}$
1.950–2.025	1290	53 ± 16	$1.48^{+0.16+0.06}_{-0.14-0.05}$
2.025–2.100	1328	63 ± 14	$1.39^{+0.15+0.07}_{-0.14-0.07}$
2.100–2.200	1444	118 ± 28	$1.26^{+0.14+0.10}_{-0.13-0.09}$
2.200–2.400	1160	126 ± 26	$1.04^{+0.16+0.10}_{-0.16-0.10}$
2.400–3.000	879	122 ± 22	$1.04^{+0.24+0.15}_{-0.25-0.15}$

procedure described in Sec. IV D. The distributions are fit to Eq. (5) with two free parameters: A (the overall normalization) and $|G_E/G_M|$. The functions H_M and H_E are replaced by the histograms obtained from MC simulation with the $p\bar{p}\gamma$ selection criteria applied.

Imperfect simulation of PID, tracking, and photon efficiency may lead to a data-simulation difference in the angular dependence of the detection efficiency. The efficiency corrections for the data-simulation differences are discussed in Sec. VI. They are applied to the angular distributions obtained from simulation. It should be noted that the corrections change the shape of the angular distributions very little. This is demonstrated in Fig. 8, where the angular dependence of the detection efficiency before and after the corrections is shown. The deviations from uniform efficiency, which do not exceed 10%, arise from the momentum dependence of proton/antiproton particle identification efficiency. A more detailed description of the fitting procedure can be found in Ref. [1].

The fit results are shown in Fig. 7 as histograms. The obtained $|G_E/G_M|$ values are listed in Table IV and shown in Fig. 9. The curve in Fig. 9 $[1 + ax/(1 + bx^3)]$, where $x = M_{p\bar{p}} - 2m_p$ GeV/ c^2 is used to determine the detection efficiency (see Sec. VI). The quoted errors on $|G_E/G_M|$ are statistical and systematic, respectively. The dominant contribution to the systematic error is due to the uncertainty in the $p\bar{p}\pi^0$ background.

The only previous measurement of the $|G_E/G_M|$ ratio comes from the PS170 experiment [12]. The ratio was measured at five points between 1.92 GeV/ c^2 and 2.04 GeV/ c^2 with an accuracy of 30%–40% (see Fig. 9). For all points it was found to be consistent with unity. The average of the PS170 measurements evaluated under the assumption that the errors are purely statistical is 0.90 ± 0.14 . The BABAR results are significantly larger for $M_{p\bar{p}} < 2.1$ GeV/ c^2 , and extend the measurements up to 3 GeV/ c^2 .

We also search for an asymmetry in the proton angular distribution. The lowest-order one-photon mechanism for proton-antiproton production predicts a symmetric angular distribution. An asymmetry arises from higher-order contributions, in particular from two-photon exchange. Two-photon exchange is discussed (see, for example, Ref. [22]) as a possible source of the difference observed in ep scattering between the G_E/G_M measurements obtained with two different experimental techniques, namely the Rosenbluth method [23], which uses the analysis of angular distributions, and the polarization method [24–26], which is based on the measurement of the ratio of the transverse and longitudinal polarization of the recoil proton.

A search for an asymmetry using previous BABAR $e^+e^- \rightarrow p\bar{p}\gamma$ results [1] is described in Ref. [27]. No asymmetry was observed within the statistical error of 2%. It should be noted that the authors of Ref. [27] did

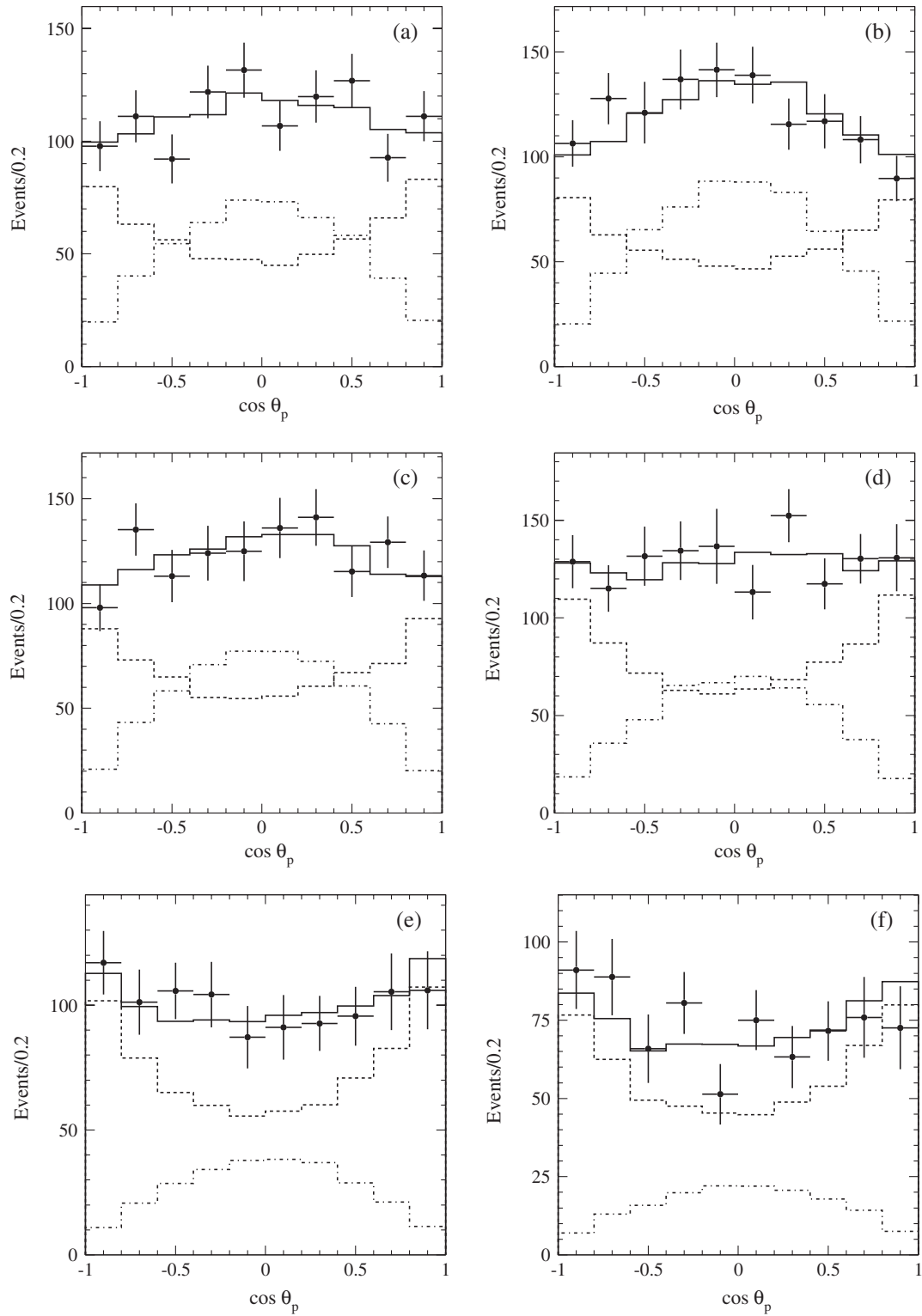


FIG. 7. The $\cos \theta_p$ distributions for different $p\bar{p}$ mass regions: (a) 1.877–1.950 GeV/c^2 , (b) 1.950–2.025 GeV/c^2 , (c) 2.025–2.100 GeV/c^2 , (d) 2.100–2.200 GeV/c^2 , (e) 2.200–2.400 GeV/c^2 , (f) 2.400–3.000 GeV/c^2 . The points with error bars show the data distributions after background subtraction. The histograms result from the fits: the dashed histograms correspond to the magnetic form factor contributions and the dot-dashed histograms to the electric form factor contributions.

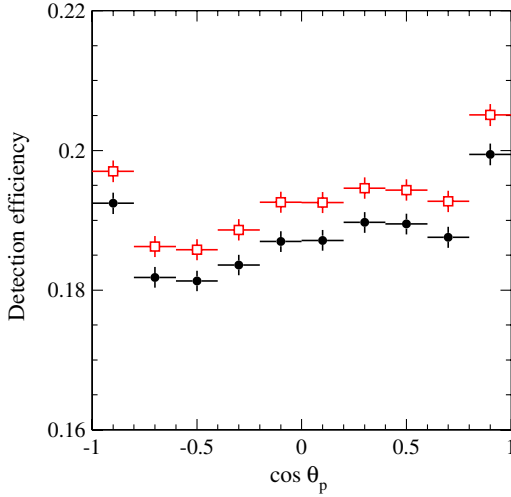


FIG. 8 (color online). The angular dependence of the detection efficiency for simulated events with $M_{p\bar{p}} < 2.5 \text{ GeV}/c^2$ before (open squares) and after (filled circles) correction for data-simulation differences in detector response.

not take into account the angular asymmetry of the detection efficiency, which is seen in Fig. 8 and in a similar plot in Ref. [1].

To measure the asymmetry we use the data with $p\bar{p}$ mass less than $3 \text{ GeV}/c^2$. The $\cos \theta_p$ distribution is fitted as described above, and the result is shown in Fig. 10. Since the MC simulation uses a model with one-photon exchange, the asymmetry in the fitted histogram is due to the asymmetry in the detection efficiency. To remove detector effects we take the ratio of the data distribution to the fitted simulated distribution. This ratio is shown in Fig. 11. A fit of a linear function to the data yields a slope

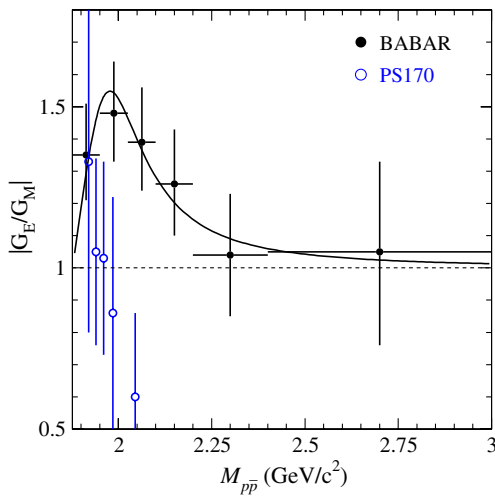


FIG. 9 (color online). The measured $|G_E/G_M|$ mass dependence. Filled circles depict *BABAR* data. Open circles show PS170 data [12]. The curve is the result of the fit described in the text.

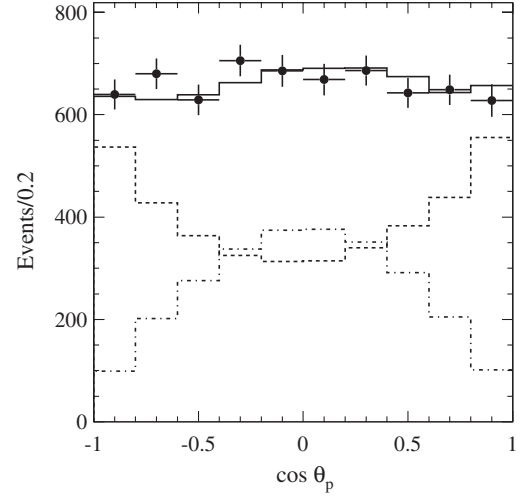


FIG. 10. The $\cos \theta_p$ distribution for the mass region from threshold to $3 \text{ GeV}/c^2$. The points with error bars show the data distribution after background subtraction; the solid histogram is the fit result. The dashed and dot-dashed histograms show the contributions of the terms corresponding to the magnetic and electric form factors, respectively.

parameter value $-0.041 \pm 0.026 \pm 0.005$. The systematic error on the slope is estimated conservatively as the maximum slope given by an efficiency correction. The correction for the data-simulation difference in antiproton nuclear interactions (see Sec. VI) is found to yield the largest angular variation.

We then calculate the integral asymmetry

$$A_{\cos \theta_p} = \frac{\sigma(\cos \theta_p > 0) - \sigma(\cos \theta_p < 0)}{\sigma(\cos \theta_p > 0) + \sigma(\cos \theta_p < 0)} = -0.025 \pm 0.014 \pm 0.003, \quad (6)$$

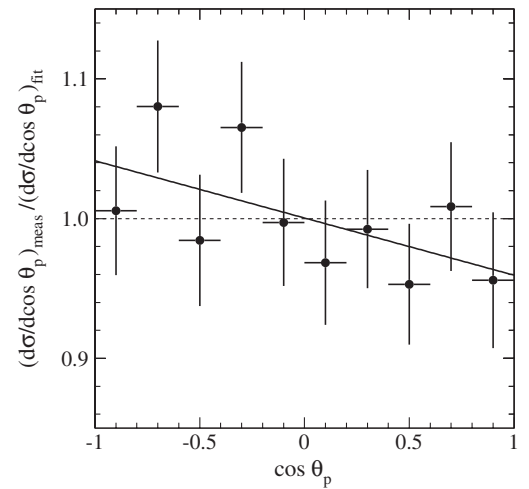


FIG. 11. The ratio of the data distribution from Fig. 10 to the fitted simulated distribution. The line shows the result of the fit of a linear function to the data points.

where $\sigma(\cos \theta_p > 0)$ and $\sigma(\cos \theta_p < 0)$ are the cross sections for $e^+e^- \rightarrow p\bar{p}\gamma$ events with $M_{p\bar{p}} < 3 \text{ GeV}/c^2$ integrated over the angular regions with $\cos \theta_p > 0$ and $\cos \theta_p < 0$, respectively. The fitted slope value and the integral asymmetry are consistent with zero. The value of the asymmetry extracted from experiment depends on the selection criteria used, in particular, on the effective energy limit for an extra photon emitted from the initial or final state. In our analysis, this limit is determined by the condition $\chi_p^2 < 30$ and is about 100 MeV.

VI. DETECTION EFFICIENCY

The detection efficiency, which is determined using MC simulation, is the ratio of true $p\bar{p}$ mass distributions obtained after and before applying the selection criteria. Since the $e^+e^- \rightarrow p\bar{p}\gamma$ differential cross section depends on two form factors, the detection efficiency cannot be determined in a model-independent way. For $M_{p\bar{p}} < 3 \text{ GeV}/c^2$, we use a model with the $|G_E/G_M|$ ratio obtained from the fits to the experimental angular distributions (curve in Fig. 9). The model error due to the uncertainty in the measured $|G_E/G_M|$ ratio is estimated to be below 1%. For $M_{p\bar{p}} > 3 \text{ GeV}/c^2$, where the $|G_E/G_M|$ ratio is not measured, a model with $|G_E/G_M| = 1$ is used. The model uncertainty for this mass region is estimated as the maximum difference between the detection efficiencies obtained with $G_E = 0$ or $G_M = 0$, and the efficiency for $|G_E/G_M| = 1$. The uncertainty does not exceed 4%. The mass dependence of the detection efficiency is shown in Fig. 12.

The efficiency determined from MC simulation (ε_{MC}) is corrected for data-simulation differences in detector response:

$$\varepsilon = \varepsilon_{\text{MC}} \prod (1 + \delta_i), \quad (7)$$

where the δ_i are efficiency corrections. They are summarized in Table V. Procedures for determining most of the

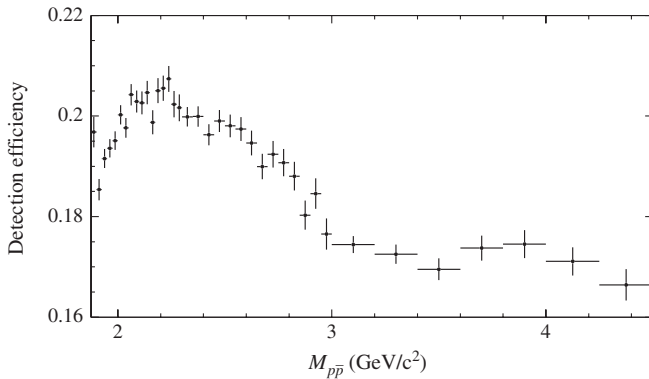


FIG. 12. The $p\bar{p}$ mass dependence of the detection efficiency obtained from MC simulation.

TABLE V. The values of the different efficiency corrections δ_i for $p\bar{p}$ invariant mass 1.9, 3.0, and 4.5 GeV/c^2 .

Effect	$\delta_i(1.9) [\%]$	$\delta_i(3) [\%]$	$\delta_i(4.5) [\%]$
$\chi_p^2 < 30$	-0.5 ± 0.1	-0.9 ± 0.1	-1.5 ± 0.2
$\chi_k^2 > 30$	0.0 ± 0.4	0.0 ± 0.4	0.0 ± 0.4
Track overlap	0.0 ± 1.5	\dots	\dots
Nuclear interaction	0.8 ± 0.4	1.1 ± 0.4	1.0 ± 0.4
Track reconstruction	0.0 ± 0.5	0.0 ± 0.5	0.0 ± 0.5
PID	-1.9 ± 2.0	-1.9 ± 2.0	-1.9 ± 2.0
Photon inefficiency	-1.9 ± 0.1	-1.7 ± 0.1	-1.7 ± 0.1
Trigger and filters	-0.7 ± 0.6	-0.1 ± 0.5	-0.1 ± 0.5
Total	-4.2 ± 2.6	-3.5 ± 2.2	-4.2 ± 2.2

efficiency corrections are described in Ref. [1]. Higher statistics and better understanding of detector performance allow us to decrease the uncertainties on the corrections for imperfect simulation of χ^2 distributions, track reconstruction, and PID. The PID procedure in this analysis differs from that used in Ref. [1]. This leads to a significant change of the PID correction value. The correction for photon inefficiency listed in Table V is a sum of corrections for calorimeter inefficiency (mainly due to dead calorimeter channels) and photon conversion in the detector material before the DCH. The latter correction, which is about -0.4% , was determined in the previous analysis [1] with the wrong sign.

A new effect studied in this analysis is track overlap in the DCH. The effect of track overlap can be observed in the distribution of the parameter $\Delta\varphi_{\pm} = \varphi_+ - \varphi_-$, where φ_+ and φ_- are the azimuthal angles at the production vertex of positive and negative tracks, respectively. The detection efficiency for simulated $e^+e^- \rightarrow p\bar{p}\gamma$ events as a function of $\Delta\varphi_{\pm}$ is shown in Fig. 13.

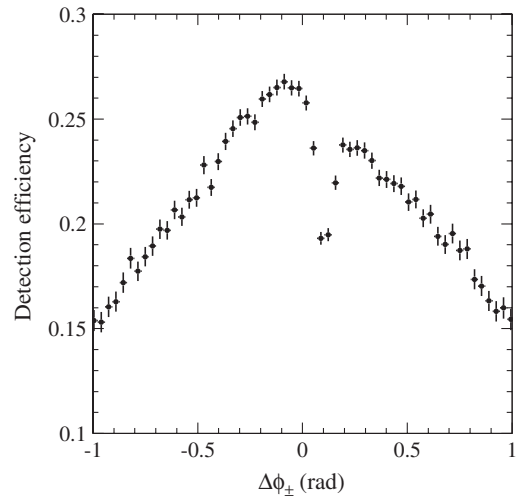


FIG. 13. The detection efficiency for $e^+e^- \rightarrow p\bar{p}\gamma$ events as a function of $\Delta\varphi_{\pm}$ obtained from MC simulation.

The z component of the *BABAR* magnetic field lies in the direction of the positive z axis, so that in the x - y plane viewed from positive z positively charged tracks experience clockwise bending and negatively charged tracks counter-clockwise bending. As a result, events with $\Delta\varphi_{\pm} > 0$

exhibit a “fishtail” two-track configuration in which the tracks tend to overlap initially. This results in the dip in efficiency that is clearly seen at $\Delta\varphi_{\pm} \sim 0.1$ rad. The ratio of the number of events with $\Delta\varphi_{\pm} > 0$ to that with $\Delta\varphi_{\pm} < 0$ can be used to estimate the efficiency loss due to

TABLE VI. The $p\bar{p}$ invariant-mass interval ($M_{p\bar{p}}$), number of selected events (N) after background subtraction and mass migration, detection efficiency (ε), ISR luminosity (L), measured cross section ($\sigma_{p\bar{p}}$), and $|F_p|$, the effective form factor for $e^+e^- \rightarrow p\bar{p}$. The contributions from $J/\psi \rightarrow p\bar{p}$ and $\psi(2S) \rightarrow p\bar{p}$ decays have been subtracted. The quoted uncertainties on N and σ are statistical and systematic, respectively. For the form factor, the combined uncertainty is listed.

$M_{p\bar{p}}$ [GeV/ c^2]	N	ε	L [pb $^{-1}$]	$\sigma_{p\bar{p}}$ [pb]	$ F_p $
1.877–1.900	$351 \pm 20 \pm 4$	0.189 ± 0.006	2.33	$806 \pm 46 \pm 30$	0.424 ± 0.014
1.900–1.925	$403 \pm 22 \pm 4$	0.178 ± 0.006	2.52	$906 \pm 50 \pm 32$	0.355 ± 0.012
1.925–1.950	$394 \pm 22 \pm 5$	0.184 ± 0.006	2.56	$845 \pm 47 \pm 31$	0.309 ± 0.010
1.950–1.975	$390 \pm 22 \pm 5$	0.186 ± 0.006	2.60	$817 \pm 46 \pm 30$	0.286 ± 0.010
1.975–2.000	$418 \pm 24 \pm 5$	0.187 ± 0.006	2.63	$854 \pm 48 \pm 31$	0.281 ± 0.009
2.000–2.025	$429 \pm 24 \pm 5$	0.192 ± 0.006	2.67	$842 \pm 48 \pm 30$	0.271 ± 0.009
2.025–2.050	$433 \pm 24 \pm 6$	0.191 ± 0.006	2.71	$846 \pm 48 \pm 31$	0.266 ± 0.009
2.050–2.075	$402 \pm 24 \pm 7$	0.197 ± 0.006	2.75	$750 \pm 45 \pm 28$	0.247 ± 0.009
2.075–2.100	$430 \pm 25 \pm 6$	0.196 ± 0.006	2.79	$796 \pm 46 \pm 29$	0.252 ± 0.009
2.100–2.125	$426 \pm 25 \pm 6$	0.195 ± 0.006	2.83	$779 \pm 45 \pm 29$	0.247 ± 0.008
2.125–2.150	$373 \pm 24 \pm 8$	0.197 ± 0.006	2.86	$666 \pm 43 \pm 27$	0.227 ± 0.009
2.150–2.175	$304 \pm 22 \pm 8$	0.192 ± 0.006	2.90	$551 \pm 41 \pm 24$	0.206 ± 0.009
2.175–2.200	$247 \pm 20 \pm 8$	0.198 ± 0.006	2.94	$429 \pm 35 \pm 20$	0.182 ± 0.009
2.200–2.225	$228 \pm 20 \pm 8$	0.198 ± 0.006	2.98	$390 \pm 33 \pm 19$	0.173 ± 0.008
2.225–2.250	$227 \pm 19 \pm 6$	0.200 ± 0.006	3.02	$379 \pm 32 \pm 16$	0.171 ± 0.008
2.250–2.275	$139 \pm 16 \pm 6$	0.195 ± 0.006	3.06	$234 \pm 27 \pm 13$	0.134 ± 0.009
2.275–2.300	$120 \pm 15 \pm 6$	0.195 ± 0.006	3.10	$201 \pm 25 \pm 12$	0.125 ± 0.009
2.300–2.350	$173 \pm 17 \pm 13$	0.193 ± 0.005	6.32	$143 \pm 14 \pm 12$	0.106 ± 0.007
2.350–2.400	$130 \pm 15 \pm 13$	0.193 ± 0.005	6.48	$105 \pm 12 \pm 11$	0.091 ± 0.007
2.400–2.450	$143 \pm 15 \pm 5$	0.190 ± 0.005	6.64	$115 \pm 12 \pm 6$	0.096 ± 0.006
2.450–2.500	$131 \pm 15 \pm 5$	0.192 ± 0.005	6.80	$101 \pm 11 \pm 5$	0.091 ± 0.006
2.500–2.550	$111 \pm 13 \pm 4$	0.191 ± 0.005	6.97	$84 \pm 10 \pm 4$	0.084 ± 0.005
2.550–2.600	$74 \pm 11 \pm 4$	0.191 ± 0.005	7.14	$55 \pm 8 \pm 3$	0.069 ± 0.006
2.600–2.650	$55 \pm 10 \pm 3$	0.188 ± 0.005	7.31	$40 \pm 8 \pm 3$	0.060 ± 0.006
2.650–2.700	$38 \pm 9 \pm 3$	0.183 ± 0.005	7.48	$28 \pm 6 \pm 3$	0.050 ± 0.006
2.700–2.750	$50 \pm 9 \pm 3$	0.186 ± 0.005	7.66	$36 \pm 7 \pm 3$	0.058 ± 0.006
2.750–2.800	$42 \pm 9 \pm 3$	0.184 ± 0.005	7.84	$29 \pm 6 \pm 3$	0.053 ± 0.006
2.800–2.850	$25 \pm 7 \pm 2$	0.181 ± 0.005	8.01	$18 \pm 5 \pm 1$	0.042 ± 0.006
2.850–2.900	$38 \pm 8 \pm 2$	0.174 ± 0.005	8.20	$27 \pm 6 \pm 2$	0.052 ± 0.006
2.900–2.950	$28 \pm 7 \pm 2$	0.178 ± 0.005	8.38	$19 \pm 5 \pm 2$	0.044 ± 0.006
2.950–3.000	$29 \pm 7 \pm 2$	0.170 ± 0.005	8.57	$20 \pm 5 \pm 2$	0.046 ± 0.006
3.000–3.200	$25 \pm 12 \pm 9$	0.168 ± 0.008	36.19	$4.2 \pm 2.0 \pm 1.6$	0.022 ± 0.007
3.200–3.400	$36 \pm 8 \pm 7$	0.166 ± 0.008	39.40	$5.4 \pm 1.2 \pm 1.1$	0.027 ± 0.004
3.400–3.600	$11 \pm 4 \pm 2$	0.163 ± 0.008	42.81	$1.6 \pm 0.6 \pm 0.3$	0.015 ± 0.003
3.600–3.800	$15 \pm 6 \pm 2$	0.167 ± 0.008	46.44	$1.9 \pm 0.8 \pm 0.3$	0.018 ± 0.004
3.800–4.000	$1 \pm 3 \pm 2$	0.168 ± 0.008	50.33	$0.2 \pm 0.4 \pm 0.2$	0.005 ± 0.005
4.000–4.250	$4 \pm 3 \pm 2$	0.164 ± 0.008	68.83	$0.3 \pm 0.3 \pm 0.2$	$0.008^{+0.004}_{-0.008}$
4.250–4.500	$3 \pm 4 \pm 2$	0.160 ± 0.008	76.00	$0.3 \pm 0.3 \pm 0.2$	$0.008^{+0.004}_{-0.008}$

track overlap. This efficiency loss reaches about 10% near the $p\bar{p}$ threshold and decreases to a negligible level for $M_{p\bar{p}}$ above $2.4 \text{ GeV}/c^2$. The effect is reproduced reasonably well by the MC simulation; data-simulation differences in the efficiency loss averaged over the mass region of maximum inefficiency, $M_{p\bar{p}} < 2.3 \text{ GeV}/c^2$, is about $(1.2 \pm 1.3)\%$. We introduce no correction for this difference. For the mass region $M_{p\bar{p}} < 2.3 \text{ GeV}/c^2$, where the effect is large, a systematic uncertainty of 1.5% is assigned to the measured cross section.

The corrected detection efficiency values are listed in Table VI. The uncertainty in detection efficiency includes simulation statistical error, model uncertainty, and the uncertainty on the efficiency correction.

VII. THE $e^+e^- \rightarrow p\bar{p}$ CROSS SECTION AND THE PROTON FORM FACTOR

The cross section for $e^+e^- \rightarrow p\bar{p}$ is calculated as

$$\sigma_{p\bar{p}}(M_{p\bar{p}}) = \frac{(dN/dM_{p\bar{p}})_{\text{corr}}}{\varepsilon R dL/dM_{p\bar{p}}}, \quad (8)$$

where $(dN/dM_{p\bar{p}})_{\text{corr}}$ is the mass spectrum corrected for resolution effects, $dL/dM_{p\bar{p}}$ is the ISR differential luminosity, $\varepsilon(M_{p\bar{p}})$ is the detection efficiency as a function of mass, and R is a radiative correction factor accounting for the Born mass spectrum distortion due to the contribution of higher-order diagrams. The ISR luminosity is calculated using the total integrated luminosity L and the integral over $\cos\theta_\gamma^*$ of the probability density function for ISR photon emission [2]:

$$\frac{dL}{dM_{p\bar{p}}} = \frac{\alpha}{\pi x} \left((2 - 2x + x^2) \log \frac{1+B}{1-B} - x^2 C \right) \frac{2M_{p\bar{p}}}{s} L. \quad (9)$$

Here $B = \cos\theta_0^*$, and θ_0^* determines the range of polar angles for the ISR photon in the e^+e^- c.m. frame: $\theta_0^* < \theta_\gamma^* < 180^\circ - \theta_0^*$. In our case $\theta_0^* = 20^\circ$, since we determine detector efficiency using simulation with $20^\circ < \theta_\gamma^* < 160^\circ$. The values of ISR luminosity integrated over the $M_{p\bar{p}}$ intervals are listed in Table VI.

The radiative correction factor R was determined in Ref. [1] with a theoretical uncertainty of 1%. Its value varies from 1.001 at $p\bar{p}$ threshold to 1.02 at $M_{p\bar{p}} = 4.5 \text{ GeV}/c^2$. The radiative correction factor does not take into account vacuum polarization; the contribution of the latter is included in the measured cross section.

The resolution-corrected mass spectrum is obtained by unfolding the mass resolution from the measured mass spectrum as described in Ref. [1]. Since the chosen mass-interval width significantly exceeds the mass resolution for all $p\bar{p}$ masses, the unfolding procedure changes the shape of the mass distribution insignificantly, but increases the uncertainties (by $\approx 20\%$) and their correlations.

After applying the unfolding procedure, the number of events in each mass interval is listed in Table VI.

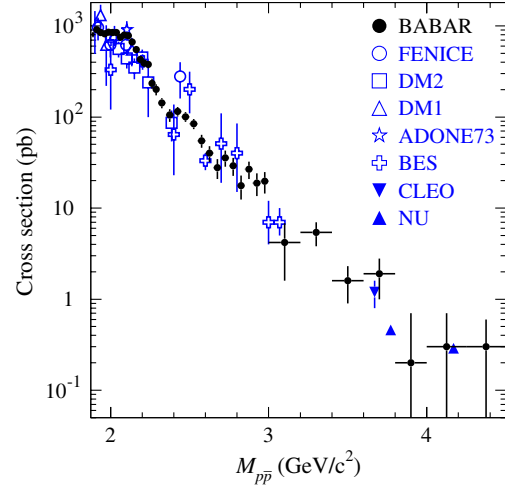


FIG. 14 (color online). The $e^+e^- \rightarrow p\bar{p}$ cross section measured in this analysis and in other e^+e^- experiments: FENICE [7], DM2 [6], DM1 [5], ADONE73 [8], BES [9], CLEO [10], and NU [11]. The contributions of $J/\psi \rightarrow p\bar{p}$ and $\psi(2S) \rightarrow p\bar{p}$ decays to the BABAR measurement have been subtracted.

The quoted errors are statistical and systematic, respectively. The latter is due to the uncertainty in background subtraction. The calculated cross section for $e^+e^- \rightarrow p\bar{p}$ is shown in Fig. 14 and listed in Table VI. For the mass intervals $3\text{--}3.2 \text{ GeV}/c^2$ and $3.6\text{--}3.8 \text{ GeV}/c^2$, the nonresonant cross section is quoted after excluding the J/ψ and $\psi(2S)$ contributions. The errors quoted are statistical and systematic. The systematic uncertainty includes the uncertainty on the number of signal events, detection efficiency, the total integrated luminosity (1%), and the radiative corrections (1%). A comparison of this result with the available e^+e^- data is shown in Fig. 14, and the behavior in the near-threshold region is shown in Fig. 15.

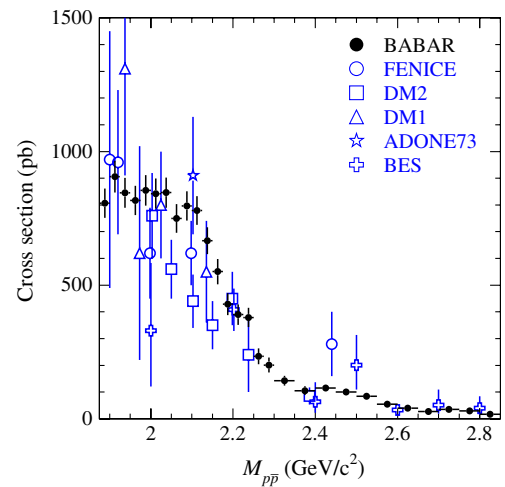


FIG. 15 (color online). The $e^+e^- \rightarrow p\bar{p}$ cross section near threshold measured in this analysis and in other e^+e^- experiments: FENICE [7], DM2 [6], DM1 [5], ADONE73 [8], and BES [9].

From the measured cross section we extract the effective form factor introduced in Eq. (3). The definition of the form factor permits comparison of our measurement with measurements from other experiments, most of which were made under the assumption $|G_E| = |G_M|$. The mass dependence of the effective form factor is shown in Fig. 16 (linear scale) and Fig. 17 (logarithmic scale), while numerical values are listed in Table VI. These form factor values are obtained as averages over mass-interval width. The four measurements from PS170 [12] with the lowest mass are located within the first mass interval of Table VI. Consequently, for the mass region near threshold, where the results from PS170 indicate that the form factor changes rapidly with mass, we calculate the cross section and effective form factor using a smaller mass-interval size. These results are listed in Table VII and shown in Fig. 18. From Figs. 16–18, it is evident that the *BABAR* effective form factor results are in reasonable agreement with, and in general more precise than, those from previous experiments. However, in the region 1.88–2.15 GeV/c^2 , the *BABAR* results are systematically above those from the other experiments.

The form factor has a complex mass dependence. The significant increase in the form factor as the $p\bar{p}$ threshold is

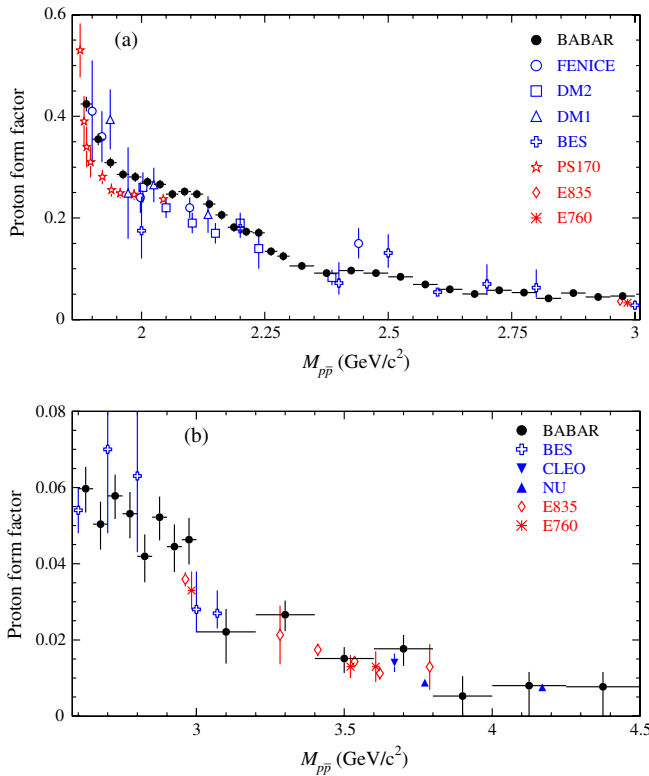


FIG. 16 (color online). The proton effective form factor measured in this analysis, in other e^+e^- experiments, and in $p\bar{p}$ experiments: FENICE [7], DM2 [6], DM1 [5], BES [9], CLEO [10], NU [11], PS170 [12], E835 [14], and E760 [13]: (a) for the mass interval from $p\bar{p}$ threshold to 3.01 GeV/c^2 , and (b) for $p\bar{p}$ masses from 2.58 to 4.50 GeV/c^2 .

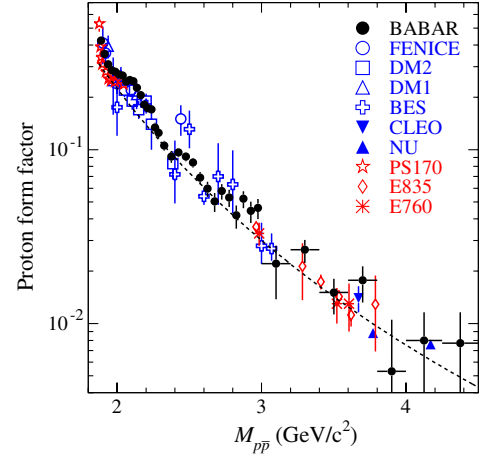


FIG. 17 (color online). The proton effective form factor measured in this analysis, in other e^+e^- experiments, and in $p\bar{p}$ experiments, shown on a logarithmic scale: FENICE [7], DM2 [6], DM1 [5], BES [9], CLEO [10], NU [11], PS170 [12], E835 [14], and E760 [13]. The curve corresponds to the QCD-motivated fit described in the text.

approached may be due to final-state interactions between the proton and antiproton [28–31]. The rapid decreases of the form factor and cross section near 2.2 GeV/c^2 , 2.55 GeV/c^2 , and 3 GeV/c^2 have not been discussed in the literature. The form-factor mass dependence below 3 GeV/c^2 is not described satisfactorily by existing models (see, for example, Refs. [32–35]). The dashed curve in Fig. 17 corresponds to a fit of the asymptotic QCD dependence of the proton form factor [36],

TABLE VII. The $p\bar{p}$ invariant-mass interval ($M_{p\bar{p}}$), number of selected events (N) after background subtraction and mass migration, measured cross section ($\sigma_{p\bar{p}}$), and effective form factor for $e^+e^- \rightarrow p\bar{p}$ ($|F_p|$). The quoted errors on N and $\sigma_{p\bar{p}}$ are statistical and systematic, respectively. For the effective form factor, the combined error is listed.

$M_{p\bar{p}}$ [GeV/c^2]	N	$\sigma_{p\bar{p}}$ [pb]	$ F_p $
1.8765–1.8800	$37 \pm 7 \pm 1$	$534 \pm 94 \pm 39$	0.515 ± 0.050
1.8800–1.8850	$80 \pm 10 \pm 1$	$826 \pm 106 \pm 42$	0.497 ± 0.034
1.8850–1.8900	$67 \pm 10 \pm 1$	$705 \pm 105 \pm 33$	0.403 ± 0.032
1.8900–1.8950	$79 \pm 11 \pm 1$	$886 \pm 121 \pm 41$	0.416 ± 0.030
1.8950–1.9000	$86 \pm 12 \pm 1$	$938 \pm 128 \pm 42$	0.404 ± 0.029
1.9000–1.9050	$70 \pm 11 \pm 1$	$785 \pm 123 \pm 35$	0.353 ± 0.029
1.9050–1.9100	$80 \pm 11 \pm 1$	$937 \pm 135 \pm 41$	0.372 ± 0.028
1.9100–1.9150	$98 \pm 13 \pm 1$	$1096 \pm 142 \pm 46$	0.390 ± 0.027
1.9150–1.9250	$156 \pm 15 \pm 2$	$862 \pm 84 \pm 32$	0.333 ± 0.017
1.9250–1.9375	$188 \pm 16 \pm 3$	$811 \pm 69 \pm 31$	0.309 ± 0.014
1.9375–1.9500	$208 \pm 17 \pm 3$	$887 \pm 72 \pm 33$	0.311 ± 0.014
1.9500–1.9625	$181 \pm 16 \pm 3$	$780 \pm 70 \pm 30$	0.283 ± 0.014
1.9625–1.9750	$209 \pm 17 \pm 3$	$850 \pm 70 \pm 32$	0.288 ± 0.013

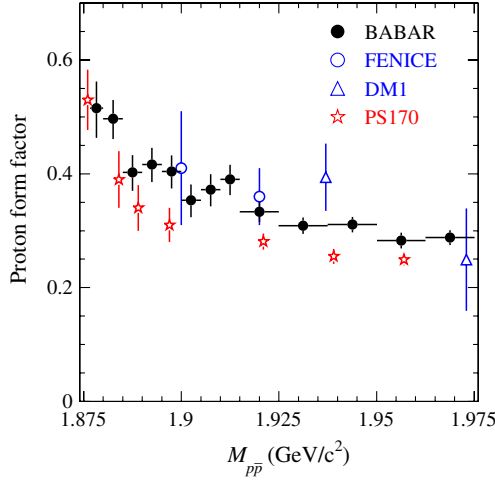


FIG. 18 (color online). The proton effective form factor near $p\bar{p}$ threshold measured in this work and in other e^+e^- and $p\bar{p}$ experiments: FENICE [7], DM1 [5], and PS170 [12].

$F_{p\bar{p}} \sim \alpha_s^2(M_{p\bar{p}}^2)/M_{p\bar{p}}^4 \sim D/(M_{p\bar{p}}^4 \log^2(M_{p\bar{p}}^2/\Lambda^2))$, to the existing data with $M_{p\bar{p}} > 3\text{ GeV}/c^2$. Here $\Lambda = 0.3\text{ GeV}$ and D is a free fit parameter. All the data above $3\text{ GeV}/c^2$ except the two points from Ref. [11] marked “NU” are well described by this function. Adding the points from Ref. [11] changes the fit χ^2/ν from 9/16 to 41/18, where ν is the number of degrees of freedom. The measurement of Ref. [11] indicates that the form factor at $M_{p\bar{p}} \approx 4\text{ GeV}/c^2$ decreases more slowly than predicted by QCD.

VIII. THE J/ψ AND $\psi(2S)$ DECAYS TO $p\bar{p}$

The $p\bar{p}$ mass spectra for selected data events in the J/ψ and $\psi(2S)$ mass regions are shown in Fig. 19. To determine the number of resonance events, each spectrum is fit with a sum of the probability density function (PDF) for signal

and a linear background term. The signal PDF is a Breit-Wigner function convolved with a double-Gaussian function describing detector resolution. The Breit-Wigner widths and masses for the J/ψ and $\psi(2S)$ resonances are fixed at their nominal values [37]. The parameters of the resolution function are determined from simulation. To account for possible differences in detector response between data and simulation, the signal PDF obtained from simulation is modified by adding in quadrature an additional term σ_G to both standard-deviation values of the double-Gaussian resolution function, and introducing a shift of the resonance mass. The free parameters in the fit to the J/ψ mass region are the number of resonance events, σ_G , the mass shift, and two parameters describing the nonresonant background. In the fit the $\psi(2S)$ mass region, σ_G and the mass shift are fixed at the values obtained for the J/ψ .

The fit results are shown as the curves in Fig. 19. We find $N_{J/\psi} = 821 \pm 30$ and $N_{\psi(2S)} = 43.5 \pm 7.7$. The other fit parameters are $\sigma_G = 5.0 \pm 1.0\text{ MeV}/c^2$ and $M_{J/\psi} - M_{J/\psi}^{\text{MC}} = -(1.7 \pm 0.5)\text{ MeV}/c^2$. The fitted value of σ_G leads to an increase in the simulation resolution ($11\text{ MeV}/c^2$) of 10%.

The corresponding detection efficiency values are determined from MC simulation. The event generator uses experimental information to describe the angular distribution of protons in J/ψ and $\psi(2S)$ decay to $p\bar{p}$. Specifically, each distribution is described by the dependence $1 + a\cos^2\theta_p$, with $a = 0.672 \pm 0.034$ for J/ψ decay [38,39] and $a = 0.72 \pm 0.13$ for $\psi(2S)$ decay [40,41]. The model error in the detection efficiency due to the uncertainty of a is negligible. The efficiencies are found to be 0.174 ± 0.001 for J/ψ and 0.172 ± 0.001 for $\psi(2S)$. The fractional correction for the data-simulation differences discussed in Sec. VI is $-(3.6 \pm 2.2)\%$.

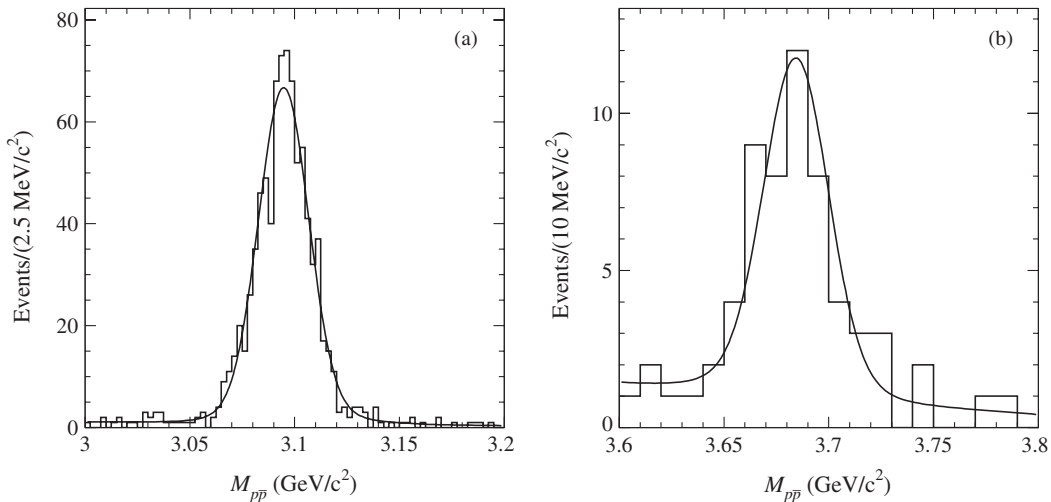


FIG. 19. The $p\bar{p}$ mass spectrum in the mass region (a) near the J/ψ , and (b) near the $\psi(2S)$. The curves display the results of the fits described in the text.

From the measured number of $\psi \rightarrow p\bar{p}$ decays in the $e^+e^- \rightarrow p\bar{p}\gamma$ reaction we can determine the product of the electronic width and the branching fraction [42]

$$\Gamma(\psi \rightarrow e^+e^-)\mathcal{B}(\psi \rightarrow p\bar{p}) = \frac{N_\psi m_\psi s}{12\pi^2 W(s, x_\psi, \theta_0^*) \varepsilon RL}, \quad (10)$$

where m_ψ is the mass of the resonance, $W(s, x_\psi, \theta_0^*)$ is the integral of $W(s, x, \theta_\gamma^*)$ [2] over $\cos \theta_\gamma^*$ (in our case $\theta_0^* = 20^\circ$), and $x_\psi = 1 - m_\psi^2/s$. The radiative-correction factor R is calculated to be 1.007 ± 0.010 for the J/ψ and 1.011 ± 0.010 for the $\psi(2S)$. From Eq. (10) we obtain

$$\begin{aligned} \Gamma(J/\psi \rightarrow e^+e^-)\mathcal{B}(J/\psi \rightarrow p\bar{p}) \\ &= (11.3 \pm 0.4 \pm 0.3) \text{ eV}, \\ \Gamma(\psi(2S) \rightarrow e^+e^-)\mathcal{B}(\psi(2S) \rightarrow p\bar{p}) \\ &= (0.67 \pm 0.12 \pm 0.02) \text{ eV}. \end{aligned} \quad (11)$$

The systematic errors include the uncertainties on the detection efficiencies, the integrated luminosity, and the radiative corrections.

Using the nominal values for the electronic widths [37], we obtain the branching fractions

$$\begin{aligned} \mathcal{B}(J/\psi \rightarrow p\bar{p}) &= (2.04 \pm 0.07 \pm 0.07) \times 10^{-3}, \\ \mathcal{B}(\psi(2S) \rightarrow p\bar{p}) &= (2.86 \pm 0.51 \pm 0.09) \times 10^{-4}. \end{aligned} \quad (12)$$

These values are in agreement with the nominal values [37] of $(2.17 \pm 0.07) \times 10^{-3}$ and $(2.76 \pm 0.12) \times 10^{-4}$, respectively, and with the recent high-precision BESIII result [43] $\mathcal{B}(J/\psi \rightarrow p\bar{p}) = (2.112 \pm 0.004 \pm 0.031) \times 10^{-3}$.

IX. SUMMARY

The process $e^+e^- \rightarrow p\bar{p}\gamma$ has been studied in the $p\bar{p}$ mass range from threshold to $4.5 \text{ GeV}/c^2$. From the measured $p\bar{p}$ mass spectrum we extract the $e^+e^- \rightarrow p\bar{p}$ cross section and determine the proton effective form factor. We have confirmed the near-threshold enhancement of the form factor observed in the PS170 experiment [12]. At higher masses the form factor has a complex steplike behavior. There are three mass regions, near $2.2 \text{ GeV}/c^2$, $2.55 \text{ GeV}/c^2$, and $3 \text{ GeV}/c^2$, that exhibit steep decreases in the form factor and cross section.

By analyzing the proton angular distributions we measure the mass dependence of the ratio $|G_E/G_M|$ for $M_{p\bar{p}}$ from threshold to $3 \text{ GeV}/c^2$. In the near-threshold region, below $2.1 \text{ GeV}/c^2$, this ratio is found to be significantly greater than unity, in disagreement with the PS170 measurement [12]. The asymmetry in the proton angular distribution is found to be

$$A_{\cos \theta_p} = -0.025 \pm 0.014 \pm 0.003$$

for $M_{p\bar{p}} < 3 \text{ GeV}/c^2$.

From the measured event yields for $e^+e^- \rightarrow J/\psi \gamma \rightarrow p\bar{p}\gamma$ and $e^+e^- \rightarrow \psi(2S)\gamma \rightarrow p\bar{p}\gamma$, we determine the branching fraction values

$$\begin{aligned} \mathcal{B}(J/\psi \rightarrow p\bar{p}) &= (2.04 \pm 0.07 \pm 0.07) \times 10^{-3}, \\ \mathcal{B}(\psi(2S) \rightarrow p\bar{p}) &= (2.86 \pm 0.51 \pm 0.09) \times 10^{-4}. \end{aligned}$$

Our results on the cross section, form factors, and J/ψ and $\psi(2S)$ decays agree with, and supersede, earlier *BABAR* measurements [1].

ACKNOWLEDGMENTS

We are grateful for the extraordinary contributions of our PEP-II colleagues in achieving the excellent luminosity and machine conditions that have made this work possible. The success of this project also relies critically on the expertise and dedication of the computing organizations that support *BABAR*. The collaborating institutions wish to thank SLAC for its support and the kind hospitality extended to them. This work is supported by the U.S. Department of Energy and National Science Foundation, the Natural Sciences and Engineering Research Council (Canada), the Commissariat à l'Energie Atomique and Institut National de Physique Nucléaire et de Physique des Particules (France), the Bundesministerium für Bildung und Forschung and Deutsche Forschungsgemeinschaft (Germany), the Istituto Nazionale di Fisica Nucleare (Italy), the Foundation for Fundamental Research on Matter (The Netherlands), the Research Council of Norway, the Ministry of Education and Science of the Russian Federation, Ministerio de Ciencia e Innovación (Spain), and the Science and Technology Facilities Council (United Kingdom). Individuals have received support from the Marie-Curie IEF program (European Union) and the A. P. Sloan Foundation (USA).

-
- [1] B. Aubert *et al.* (*BABAR* Collaboration), *Phys. Rev. D* **73**, 012005 (2006).
 - [2] G. Bonneau and F. Martin, *Nucl. Phys.* **B27**, 381 (1971).
 - [3] A. B. Arbuzov and T. V. Kopylova, *J. High Energy Phys.* **04** (2012) 009.

- [4] H. Czyz, J. H. Kühn, E. Nowak, and G. Rodrigo, *Eur. Phys. J. C* **35**, 527 (2004).
- [5] B. Delcourt *et al.* (DM1 Collaboration), *Phys. Lett.* **86B**, 395 (1979).
- [6] D. Bisello *et al.* (DM2 Collaboration), *Nucl. Phys.* **B224**, 379 (1983); *Z. Phys. C* **48**, 23 (1990).

- [7] A. Antonelli *et al.* (FENICE Collaboration), *Nucl. Phys.* **B517**, 3 (1998).
- [8] M. Castellano, G. Giugno, J. W. Humphrey, E. S. Palmieri, G. Troise, U. Troya, and S. Vitale, *Nuovo Cimento A* **14**, 1 (1973).
- [9] M. Ablikim *et al.* (BES Collaboration), *Phys. Lett. B* **630**, 14 (2005).
- [10] T. K. Pedlar *et al.* (CLEO Collaboration), *Phys. Rev. Lett.* **95**, 261803 (2005).
- [11] K. K. Seth, S. Dobbs, Z. Metreveli, A. Tomaradze, T. Xiao, and G. Bonvicini, *Phys. Rev. Lett.* **110**, 022002 (2013).
- [12] G. Bardin *et al.* (PS170 Collaboration), *Nucl. Phys.* **B411**, 3 (1994).
- [13] T. A. Armstrong *et al.* (E760 Collaboration), *Phys. Rev. Lett.* **70**, 1212 (1993).
- [14] M. Ambrogiani *et al.* (E835 Collaboration), *Phys. Rev. D* **60**, 032002 (1999); M. Andreotti *et al.*, *Phys. Lett. B* **559**, 20 (2003).
- [15] B. Aubert *et al.* (BABAR Collaboration), *Nucl. Instrum. Methods Phys. Res., Sect. A* **479**, 1 (2002).
- [16] W. Menges, *IEEE Nucl. Sci. Symp. Conf. Rec.* **5**, 1470 (2006).
- [17] H. Czyż and J. H. Kühn, *Eur. Phys. J. C* **18**, 497 (2001).
- [18] M. Caffo, H. Czyż, and E. Remiddi, *Nuovo Cimento Soc. Ital. Fis.* **110A**, 515 (1997); *Phys. Lett. B* **327**, 369 (1994).
- [19] E. Barberio and Z. Waś, *Comput. Phys. Commun.* **79**, 291 (1994).
- [20] T. Sjöstrand, *Comput. Phys. Commun.* **82**, 74 (1994).
- [21] S. Agostinelli *et al.*, *Nucl. Instrum. Methods Phys. Res., Sect. A* **506**, 250 (2003).
- [22] P. G. Blunden, W. Melnitchouk, and J. A. Tjon, *Phys. Rev. Lett.* **91**, 142304 (2003).
- [23] J. Arrington, *Phys. Rev. C* **69**, 022201 (2004).
- [24] O. Gayou *et al.*, *Phys. Rev. Lett.* **88**, 092301 (2002).
- [25] V. Punjabi *et al.*, *Phys. Rev. C* **71**, 055202 (2005); **71**, 069902(E) (2005).
- [26] A. J. R. Puckett *et al.*, *Phys. Rev. Lett.* **104**, 242301 (2010).
- [27] E. Tomasi-Gustafsson, E. A. Kuraev, S. Bakmaev, and S. Pacetti, *Phys. Lett. B* **659**, 197 (2008).
- [28] J. Haidenbauer, H.-W. Hammer, U.-G. Meißner, and A. Sibirtsev, *Phys. Lett. B* **643**, 29 (2006).
- [29] G. Y. Chen, H. R. Dong, and J. P. Ma, *Phys. Lett. B* **692**, 136 (2010).
- [30] V. F. Dmitriev and A. I. Milstein, *Nucl. Phys. B, Proc. Suppl.* **181–182**, 66 (2008).
- [31] O. D. Dalkarov, P. A. Khakhulin, and A. Y. Voronin, *Nucl. Phys.* **A833**, 104 (2010).
- [32] M. A. Belushkin, H.-W. Hammer, and U.-G. Meißner, *Phys. Rev. C* **75**, 035202 (2007).
- [33] J. P. B. C. de Melo, T. Frederico, E. Pace, S. Pisano, and G. Salmè, *Phys. Lett. B* **671**, 153 (2009).
- [34] S. Furuichi, H. Ishikawa, and K. Watanabe, *Phys. Rev. C* **81**, 045209 (2010).
- [35] E. L. Lomon and S. Pacetti, *Phys. Rev. D* **85**, 113004 (2012); **86**, 039901(E) (2012).
- [36] V. L. Chernyak and A. R. Zhitnitsky, *JETP Lett.* **25**, 510 (1977); G. P. Lepage and S. J. Brodsky, *Phys. Rev. Lett.* **43**, 545 (1979).
- [37] J. Beringer *et al.* (Particle Data Group), *Phys. Rev. D* **86**, 010001 (2012).
- [38] D. Pallin *et al.* (DM2 Collaboration), *Nucl. Phys.* **B292**, 653 (1987); R. Brandelik *et al.* (DASP Collaboration), *Z. Phys. C* **1**, 233 (1979); I. Peruzzi *et al.* (MARK I Collaboration), *Phys. Rev. D* **17**, 2901 (1978); M. W. Eaton *et al.* (MARK II Collaboration), *Phys. Rev. D* **29**, 804 (1984).
- [39] J. Z. Bai *et al.* (BES Collaboration), *Phys. Lett. B* **591**, 42 (2004).
- [40] M. Ambrogiani *et al.* (E835 Collaboration), *Phys. Lett. B* **610**, 177 (2005).
- [41] M. Ablikim *et al.* (BES Collaboration), *Phys. Lett. B* **648**, 149 (2007).
- [42] M. Benayoun, S. I. Eidelman, V. N. Ivanchenko, and Z. K. Silagadze, *Mod. Phys. Lett. A* **14**, 2605 (1999).
- [43] M. Ablikim *et al.* (BESIII Collaboration), *Phys. Rev. D* **86**, 032014 (2012).